Free and Forced Vibration Analysis over Meshes with Tangled (Non-Convex) Elements

Bhagyashree Prabhune, Krishnan Suresh*

Department of Mechanical Engineering, University of Wisconsin-Madison, WI, USA

Abstract

Tangled (non-convex) elements, i.e. elements with negative Jacobian determinant, can lead to erroneous results in the standard finite element method (FEM). Constructing tangle-free, well-structured meshes for complex geometries is often impossible. Hence there is a need to explore analysis methods that can directly handle such tangled meshes.

In this paper, we propose the isoparametric tangled finite element method (i-TFEM) for free and forced vibration problems over tangled meshes. By employing piece-wise invertible mapping, a variational formulation is derived, leading to a simple modification of the standard FEM stiffness and mass matrices with the incorporation of additional compatibility constraints. Moreover, i-TFEM reduces to standard FEM for non-tangled (regular) meshes. The proposed method is implemented for three types of elements: 4-node quadrilateral, 9-node quadrilateral, and 8-node hexahedral elements. The numerical results demonstrate that i-TFEM is able to consistently handle general tangled (non-convex) elements, enabling convenient meshing for complex geometries.

Keywords: Tangled finite element method (i-TFEM), Elastodynamics, Tangled Mesh, Negative Jacobian, Non-convex elements, Mixed finite element, Algebraic constraints, Generalized Eigen-value

1. Introduction

Finite element method (FEM) is a widely used numerical technique to study the dynamic response of the structures. Despite numerous advances in the FEM, a major challenge which remains is the mesh generation for complex geometries, which can be excessively time-consuming, accounting for over 80% of the overall analysis time [1]. This challenge arises due to the strict topological and geometric requirements that must be satisfied by the mesh: (1) the mesh must be tangle-free, (2) the elements must exhibit high quality, (3) the mesh must conform to the geometry, and (4) must be well-structured. Meeting all these constraints is a non-trivial task.

The first requirement, tangle-free elements, necessitates that the Jacobian determinant remains positive throughout the entire mesh. Fig. 1a and Fig. 1b illustrate examples of tangled meshes with 8-node hexahedral and 9-node quadrilateral elements respectively. If a mesh contains even a single tangled element, it is considered invalid or unacceptable for FEM. To quote [2]: *"Because tangled meshes generate physically*

*Corresponding author

Email addresses: bprabhune@wisc.edu (Bhagyashree Prabhune), ksuresh@wisc.edu (Krishnan Suresh)

invalid solutions, it is imperative that such meshes are untangled".

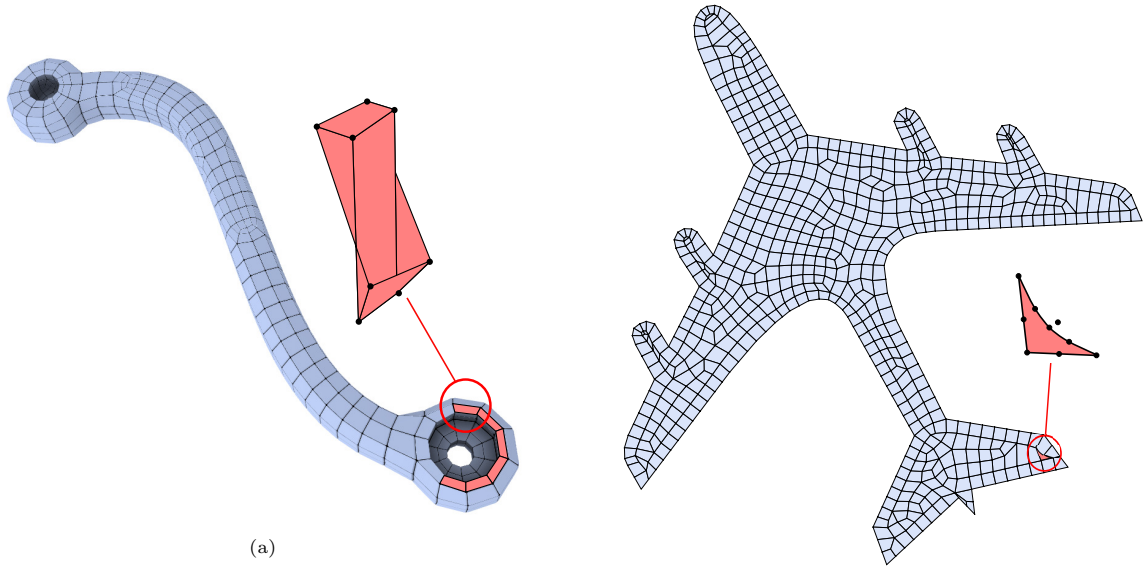

(a) (b)

Figure 1: (a) Tangled mesh with 8-node hexahedral elements; the mesh has been provided in [3]. (b) Tangled mesh with 9-node quadrilateral elements; the mesh has been generated using the algorithm presented in [4]; Highlighted elements are tangled (negative Jacobian elements).

Unfortunately, mesh generators often struggle to produce tangle-free meshes [5, 6]. In an attempt to meet quality requirements, geometric conformance, and topological constraints (i.e. requirements 2-4 mentioned previously), many state-of-the-art mesh generation algorithms, such as Polycube mapping and frame-field based methods, end up producing tangled meshes [7, 8, 9, 8, 10, 11, 12, 13, 14, 15, 16, 17]. This issue is particularly severe with 3D hexahedral meshes, as highlighted in [5], stating, *"maintaining the inversion-free (tangle-free) property of hex-mesh poses a great challenge"*. Apart from mesh generation, tangled meshes also arise during shape optimization [18], large deformation simulations [19, 20], and mesh morphing [21].

Numerous untangling algorithms have been developed to tackle these challenges [22, 23, 3]. However, untangling is not always guaranteed, as reported in multiple instances where no tangle-free solution is possible [3, 24, 23, 25]. To quote [25], *"... it is probably impossible to untangle the mesh under these hard constraints."* In fact, certain topological structures may not have an untangled mesh solution [3, 26]. Moreover, there are no known a priori tests to determine if a mesh can be untangled [27]. Finally, untangling can be expensive, and can pose challenges in mapping simulation data.

Non-traditional methods developed to tackle meshing challenges include smoothed finite element (SFEM) [28], overlapping finite elements [29, 30, 31], polygonal finite element methods (PFEM) [32, 33, 34, 35], virtual element method (VEM) [36, 37, 38, 39, 40], unsymmetric finite element [41, 42]. These methods partly relax one or more meshing constraints (discussed at the beginning of the section). For instance, the overlapping finite element method allows highly distorted elements, i.e. requirement 2 mentioned previously.

The unsymmetric FEM relaxes the constraints related to tangling (requirement 1) and mesh distortion (requirement 2). Similarly, methods such as SFEM and VEM offer flexibility in element shapes (requirements 1 and 2) [43, 44, 45] and allow hanging nodes (requirement 4) [46, 47, 48]. While the non-traditional methods provide promising solutions, meshing (tangling) challenges persist. These methods have limitations in terms of the configurations they can handle. For instance, practical meshes generated from state-of-the-art mesh generation algorithms, often contain 'self-penetrating' tangled elements [49], which are not addressed by these approaches. Additionally, it is difficult to integrate many of these methods with existing FEM framework.

Recently, an isoparametric tangled finite element method (i-TFEM) [49, 50, 51, 51, 52, 53] was proposed which specifically addresses tangled elements (mesh requirement 1) by modifying traditional FEM. I-TFEM reduces to standard FEM for non-tangled meshes and requires minimal changes to the existing FEM framework. It can effectively handle real-world tangled meshes generated by the state-of-the-art mesh generation methods such as Polycube mapping [10, 11, 12] and frame-field [17] based approaches. I-TFEM has been demonstrated for linear and non-linear static elasticity and Poisson problems over tangled meshes.

In this study, i-TFEM is extended to free and forced vibration problems, in both 2D and 3D. The paper presents a detailed variational formulation with examples covering three element types: 4-node and 9-node quadrilateral, as well as 8-node hexahedral elements. The proposed method uses the same basis functions as standard FEM, and handles tangled elements by incorporating the *field compatibility* constraints. The computation of stiffness and mass matrices in i-TFEM is same as in standard FEM, allowing easy implementation in the existing FEM software. Numerous real-world and synthetically generated meshes are considered to demonstrate the efficiency and robustness of the method.

The remainder of this paper is organized as follows: Section 2 addresses basic i-TFEM formulation, while Section 3 details the elastodynamic variational formulation for i-TFEM. Implementation details are provided in Section 4, followed by numerical results in Section 5. Finally, Section 6 presents concluding remarks.

2. Isoparametric TFEM

We provide here a brief review of important i-TFEM concepts [50, 53, 52] using a tangled 9-noded quadrilateral element (other elements are discussed later on). We consider an element to be tangled if the Jacobian determinant ($|\boldsymbol{J}|$) at any of the quadrature points is negative. Note that elements with zero Jacobian at quadrature points are not addressed here. Consider the tangled Q9 element in the physical space (x_1, x_2) in Fig. 2a, and the parametric mapping ϕ from the (ξ_1, ξ_2) space in Fig. 2b to the tangled element. Observe that the mapping is non-invertible, i.e., there are distinct points ($\boldsymbol{a}$ and $\boldsymbol{b}$) in the parametric space that map to the same physical point ($\boldsymbol{p}$); such physical points lie outside the element. In other words, the element folds onto itself, creating an overlapping region, also referred to as the fold F (see Fig. 2c). Furthermore, at points such as $\boldsymbol{a}$, the determinant of the Jacobian is negative, while at $\boldsymbol{b}$, the determinant is positive. Thus, one can divide the parametric space into positive and negative regions denoted by J^+

and J^- respectively. The corresponding regions in the physical space are referred to as positive (C^+) and negative (C^-) components respectively.

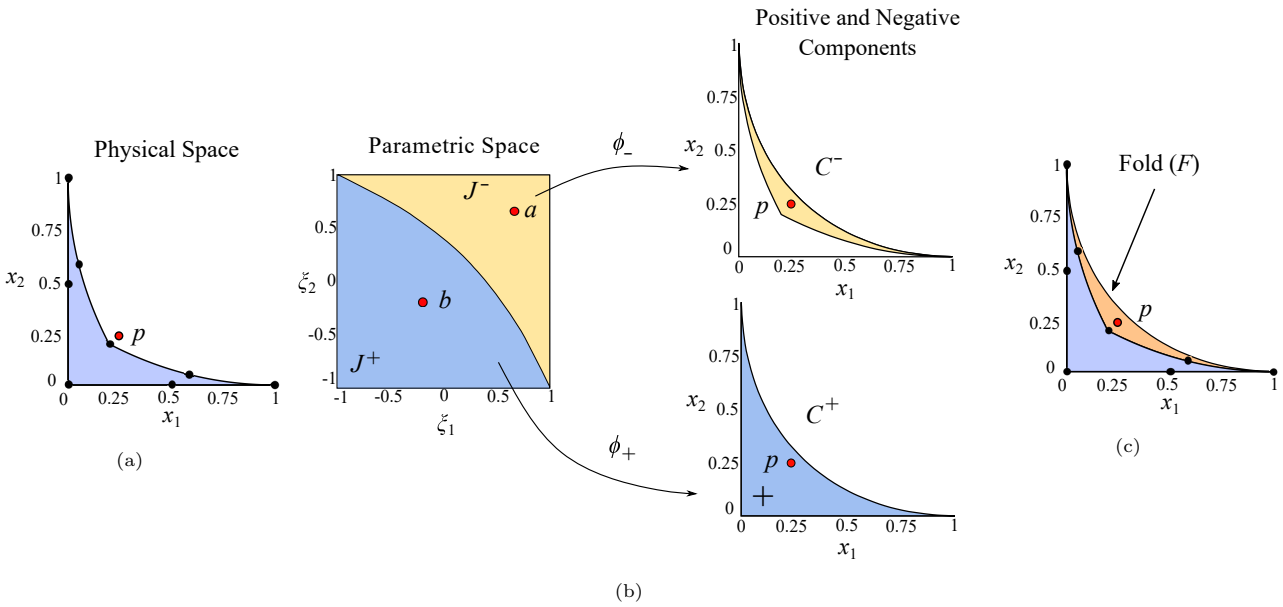

Figure 2: (a) Physical space of the tangled Q9 element. (b) Parametric space of the tangled element, that can be divided into positive and negative Jacobian regions.Corresponding physical space with positive and negative components. (c) The overlapping region or fold F_1 of the tangled element.

The main idea in i-TFEM is to treat the positive and negative Jacobian regions (J^+ and J^-) separately during stiffness matrix computation since the two independent mappings

$$\phi_\pm \colon J^\pm \to C^\pm$$

are both invertible. This will also lead us to a few definitions.

For a tangled element E_j, let $\boldsymbol{N}_j(\boldsymbol{\xi})$ be the standard shape functions (i.e., biquadratic Lagrange shape functions for Q9 element) defined over the parametric space. Now, let $\boldsymbol{N}_j^\pm$ be the restriction of $\boldsymbol{N}_j$ to $J^\pm$, i.e.,

$$\boldsymbol{N}_j^\pm(\boldsymbol{x}) \coloneqq \boldsymbol{N}_j(\phi_\pm^{-1}(\boldsymbol{x})) \tag{1}$$

The corresponding displacement fields defined over $C_j^\pm$ are defined as:

$$\boldsymbol{u}_j^\pm(\boldsymbol{x}) \coloneqq \boldsymbol{N}_j^\pm(\boldsymbol{x})\boldsymbol{d}_j \tag{2}$$

where $\boldsymbol{d}_j$ is the displacement vector for j^{th} element. The components C_j^+ and C_j^- overlap, creating a folded region $F_j = C_j^+ \cap C_j^-$. To impose uniqueness of the field in the folded region, a *field compatibility constraint* is enforced in i-TFEM (also see [50] for additional explanation and [54] for treatment on displacement constraints) :

$$\boldsymbol{u}_j^+(\boldsymbol{x}) - \boldsymbol{u}_j^-(\boldsymbol{x}) = 0, \quad \forall \boldsymbol{x} \in F_j. \tag{3}$$

Introducing the notation $[\![\cdot]\!] = (\cdot)^+ - (\cdot)^-$, the above constraint can be written as:

$$[\![\boldsymbol{u}_j]\!] = 0 \quad \text{in } F_j \tag{4}$$

Now consider the two-element mesh shown in Fig. 3a (the central nodes are not shown to avoid clutter) where one of the elements (E_1) is tangled. The positive and negative components of E_1 are shown in Fig. 3b. Element E_2 is not tangled and has only one positive component (see Fig. 3c), i.e., $E_2 = C_2^+$ while $C_2^- = \emptyset$. However, the component C_1^- overlaps with E_2 as well, i.e., the overlapping region of the tangled element (C_1^-) now intersects with E_2. Construction of the stiffness matrix, i.e., integrating shape functions and their derivatives over a tangled mesh requires careful consideration of this overlap. For example, to compute the total area of the two-element mesh, we must subtract the integral over C_1^- to avoid double-counting:

$$\int_{E_1+E_2} d\Omega = \int_{C_1^+} d\Omega + \int_{C_2^+} d\Omega - \int_{C_1^-} d\Omega \tag{5}$$

This will be relevant in the next section. Given this simple framework, one can now proceed towards applying these concepts to solve elastodynamics problems over tangled meshes.

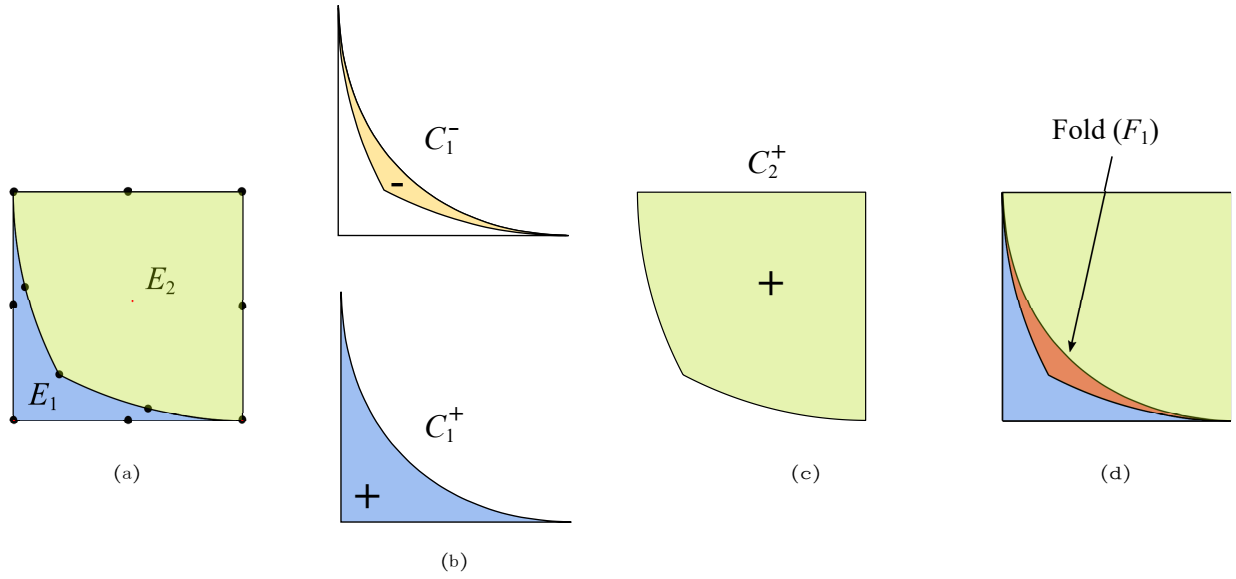

Figure 3: (a) 2-D domain discretized into two 9-node quadrilateral elements (central nodes are not shown to avoid clutter). (b) Positive and negative $|\boldsymbol{J}|$ regions of the tangled element. (c) Non-tangled element of the mesh. (d) Overlapping region intersects with the neighboring convex element.

3. i-TFEM for Elastodynamics

3.1. Weak formulation

Now consider an elastodynamics problem over a domain Ω that is discretized into m elements, some of which may be tangled (see Fig. 4). The body is subjected to body forces $\boldsymbol{b}$ and tractions $\boldsymbol{t}$ on $\partial\Omega^t$. We will assume that the field $\boldsymbol{u}$ satisfies Dirichlet boundary conditions $\boldsymbol{u}_j = \boldsymbol{u}_j^d$ over $\partial\Omega^d$.

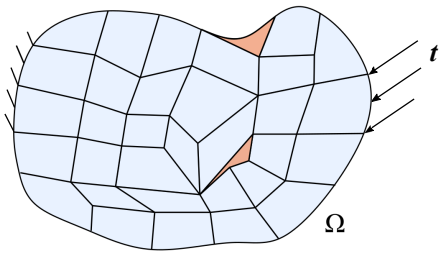

Figure 4: Domain Ω with boundary conditions and arbitrary mesh.

Let the elements be indexed by the set $I = \{1, \ldots, m\}$. Based on the principle of virtual work, recall the weak form of the governing equation for elastodynamics problems:

Find displacement $\boldsymbol{u} \in H^1$ such that

$$b(\delta \boldsymbol{u}, \rho \ddot{\boldsymbol{u}}) + a(\delta \boldsymbol{u}, \boldsymbol{u}) = f(\delta \boldsymbol{u}), \quad \forall \delta \boldsymbol{u} \in H_0^1 \tag{6}$$

$$\text{where,} \quad b(\delta \boldsymbol{u}, \rho \ddot{\boldsymbol{u}}) = \sum_{j \in I} \int_{E_j} \delta \boldsymbol{u}_j \cdot \rho \ddot{\boldsymbol{u}}_j \, \mathrm{d}\Omega \tag{6a}$$

$$a(\delta \boldsymbol{u}, \boldsymbol{u}) = \sum_{j \in I} \int_{E_j} \boldsymbol{\varepsilon}\left(\delta \boldsymbol{u}_j\right) : \boldsymbol{\sigma}\left(\boldsymbol{u}_j\right) \, \mathrm{d}\Omega \tag{6b}$$

$$f(\delta \boldsymbol{u}) = \sum_{j \in I} \int_{E_j} \delta \boldsymbol{u}_j \cdot \boldsymbol{b} \, \mathrm{d}\Omega + \sum_{j \in I} \int_{\partial E_j^t} \delta \boldsymbol{u}_j \cdot \boldsymbol{t} \, \mathrm{d}S \tag{6c}$$

where ρ is the mass density and $\ddot{\boldsymbol{u}}$ is the acceleration. Assuming linear elastic material, the stress tensor $\boldsymbol{\sigma}$ is computed using the elasticity tensor $\boldsymbol{D}$ and strain tensor $\boldsymbol{\varepsilon}$ as $\boldsymbol{\sigma} = \boldsymbol{D}\boldsymbol{\varepsilon}$.

When the mesh is tangled as in Fig. 4, the standard weak form will lead to erroneous results (demonstrated later in Section 5). To resolve this, we make two modifications. Analogous to Eq. 5, integrals over negative components are subtracted to avoid double-counting. For example, for the two-element tangled mesh, the first term of the weak form is expressed as:

$$b(\delta \boldsymbol{u}, \rho \ddot{\boldsymbol{u}}) = \int_{C_1^+} \delta \boldsymbol{u}_1^+ \cdot \rho \ddot{\boldsymbol{u}}_1^+ \mathrm{d}\Omega + \int_{C_2^+} \delta \boldsymbol{u}_2^+ \cdot \rho \ddot{\boldsymbol{u}}_2^+ \mathrm{d}\Omega - \int_{C_1^-} \delta \boldsymbol{u}_1^- \cdot \rho \ddot{\boldsymbol{u}}_1^- \mathrm{d}\Omega \tag{7}$$

This applies to all tangled elements, and to all integral terms.

Next, consider the field compatibility constraint in Eq. 4. We employ the Lagrange multiplier method [54, 55, 56, 57, 58, 59, 60] to enforce this constraint over every tangled element. For example, for the two-element mesh in Fig. 4a, we will require that:

$$\int_{F_1} \delta \boldsymbol{\lambda}_1 \cdot [\![\boldsymbol{u}_1]\!] \, \mathrm{d}\Omega = 0 \quad \forall \, \delta \boldsymbol{\lambda}_1 \in L^2, \tag{8}$$

Moreover, we must suitably modify Eq. 6 as follows:

$$b(\delta \boldsymbol{u}, \rho \ddot{\boldsymbol{u}}) + a(\delta \boldsymbol{u}, \boldsymbol{u}) + \int_{F_1} [\![\delta \boldsymbol{u}_1]\!] \cdot \boldsymbol{\lambda}_1 \, \mathrm{d}\Omega = f(\delta \boldsymbol{u}), \quad \forall \delta \boldsymbol{u} \in H_0^1.$$

We can now generalize these concepts to an arbitrary mesh. Let the tangled elements be identified by the index $I_{\text{tangled}} \subset I$. The weak form in i-TFEM can then be expressed as follows:

Find $\boldsymbol{u} \in H^1$ and $\boldsymbol{\lambda} \in L^2$ such that

$$b(\delta\boldsymbol{u}, \rho\ddot{\boldsymbol{u}}) + a(\delta\boldsymbol{u}, \boldsymbol{u}) + \sum_{j \in I_{\text{tangled}}} \int_{F_j} [\![\delta\boldsymbol{u}_j]\!] \cdot \boldsymbol{\lambda}_j \, \mathrm{d}\Omega = f(\delta\boldsymbol{u}), \quad \forall \delta\boldsymbol{u} \in H_0^1 \tag{9a}$$

$$\sum_{j \in I_{\text{tangled}}} \int_{F_j} \delta\boldsymbol{\lambda}_j \cdot [\![\boldsymbol{u}_j]\!] \, \mathrm{d}\Omega = 0, \qquad \forall \delta\boldsymbol{\lambda} \in L^2 \tag{9b}$$

where,

$$b(\delta\boldsymbol{u}, \rho\ddot{\boldsymbol{u}}) = \sum_{j \in I} \int_{C_j^+} \delta\boldsymbol{u}_j^+ \cdot \rho\ddot{\boldsymbol{u}}_j^+ \mathrm{d}\Omega - \sum_{j \in I_{\text{tangled}}} \int_{C_j^-} \delta\boldsymbol{u}_j^- \cdot \rho\ddot{\boldsymbol{u}}_j^- \mathrm{d}\Omega \tag{10a}$$

$$a(\delta\boldsymbol{u}, \boldsymbol{u}) = \sum_{j \in I} \int_{C_j^+} \boldsymbol{\varepsilon}\left(\delta\boldsymbol{u}_j^+\right) : \boldsymbol{\sigma}\left(\boldsymbol{u}_j^+\right) \mathrm{d}\Omega - \sum_{j \in I_{\text{tangled}}} \int_{C_j^-} \boldsymbol{\varepsilon}\left(\delta\boldsymbol{u}_j^-\right) : \boldsymbol{\sigma}\left(\boldsymbol{u}_j^-\right) \mathrm{d}\Omega \tag{10b}$$

$$f(\delta\boldsymbol{u}) = \sum_{j \in I} \int_{C_j^+} \delta\boldsymbol{u}_j^+ \cdot \boldsymbol{b} \mathrm{d}\Omega - \sum_{j \in I_{\text{tangled}}} \int_{C_j^-} \delta\boldsymbol{u}_j^- \cdot \boldsymbol{b} \mathrm{d}\Omega + \sum_{j \in I} \int_{\partial E_j^t} \delta\boldsymbol{u}_j \cdot \boldsymbol{t} \mathrm{d}S \tag{10c}$$

3.2. Finite element approximation

We now approximate the primary field $\boldsymbol{u}$ and the Lagrange multiplier field $\boldsymbol{\lambda}$ as follows:

$$\boldsymbol{u}_j \approx \boldsymbol{N}_j \boldsymbol{d}_j, \quad \boldsymbol{\lambda}_j \approx \boldsymbol{N}_j^{\lambda} \hat{\boldsymbol{\lambda}}_j \tag{11}$$

Adopting the (Bubnov-) Galerkin framework, Eq. 9 leads to the following system of equations:

$$\boldsymbol{M}\ddot{\boldsymbol{d}} + \boldsymbol{K}\boldsymbol{d} + \boldsymbol{S}\hat{\boldsymbol{\lambda}} = \boldsymbol{f} \tag{12a}$$

$$\boldsymbol{S}^{\top}\boldsymbol{d} = \boldsymbol{0} \tag{12b}$$

where the mass matrix is given by:

$$\boldsymbol{M} = \mathop{\mathbb{A}}_{j \in I} \int_{C_j^+} \left(\boldsymbol{N}_j^{+\top} \rho \boldsymbol{N}_j^+\right) d\Omega \quad - \mathop{\mathbb{A}}_{j \in I_{\text{tangled}}} \int_{C_j^-} \left(\boldsymbol{N}_j^{-\top} \rho \boldsymbol{N}_j^-\right) d\Omega, \tag{13}$$

the stiffness matrix is given by:

$$\boldsymbol{K} = \mathop{\mathbb{A}}_{j \in I} \int_{C_j^+} \left(\nabla \boldsymbol{N}_j^{+\top} \boldsymbol{D} \nabla \boldsymbol{N}_j^+\right) d\Omega \quad - \mathop{\mathbb{A}}_{j \in I_{\text{tangled}}} \int_{C_j^-} \left(\nabla \boldsymbol{N}_j^{-\top} \boldsymbol{D} \nabla \boldsymbol{N}_j^-\right) d\Omega, \tag{14}$$

the forcing term is given by:

$$\boldsymbol{f} = \mathop{\mathbb{A}}_{j \in I} \int_{C_j^+} \boldsymbol{N}_j^{\top} \boldsymbol{b} \, d\Omega - \mathop{\mathbb{A}}_{j \in I_{\text{tangled}}} \int_{C_j^-} \boldsymbol{N}_j^{-\top} \boldsymbol{b} \, d\Omega + \mathop{\mathbb{A}}_{j \in I} \int_{\partial E_j^t} \boldsymbol{N}_j^{\top} \boldsymbol{t} \, dS, \tag{15}$$

and the constraint matrix by:

$$\boldsymbol{S} = \mathop{\mathbb{A}}_{j \in I_{\text{tangled}}} \int_{F_j} [\![\boldsymbol{N}_j]\!]^{\top} \boldsymbol{N}^{\lambda} d\Omega = \mathop{\mathbb{A}}_{j \in I_{\text{tangled}}} \int_{F_j} \left(\boldsymbol{N}_j^+ - \boldsymbol{N}_j^-\right)^{\top} \boldsymbol{N}^{\lambda} d\Omega. \tag{16}$$

where $\mathbb{A}$ is the assembly operator. In Eq. 16, the choice of $\boldsymbol{N}^{\lambda}$ depends on the choice of $\boldsymbol{N}$, i.e., the type of element (Q4, Q9, H8, etc.); see Section 4. Further, observe that the expressions in Eq. 13 through Eq. 16 entail integration over non-convex regions (C_j^+, C_j^-, and F_j), associated with tangled elements. Fortunately, this can be circumvented, as discussed in Section 4.

One can incorporate damping with a damping matrix $\boldsymbol{C}$ and the velocity vector $\dot{\boldsymbol{d}}$ as:

$$\boldsymbol{M}\ddot{\boldsymbol{d}} + \boldsymbol{C}\dot{\boldsymbol{d}} + \boldsymbol{K}\boldsymbol{d} + \boldsymbol{S}\hat{\boldsymbol{\lambda}} = \boldsymbol{f} \tag{17a}$$

$$\boldsymbol{S}^{\top}\boldsymbol{d} = \boldsymbol{0} \tag{17b}$$

In this paper, for simplicity, Rayleigh damping is assumed, i.e., $\boldsymbol{C} = \alpha_1\boldsymbol{M} + \alpha_2\boldsymbol{K}$, where α_1 and α_2 are the Rayleigh damping coefficients.

3.3. Forced vibration

Many schemes [61, 62, 63] can be used to solve Eq. 17. In this work, we adopt the Newmark method (with implicit time integration) [63, 64] for simplicity; for the state-of-the-art time integration methods, please see [65, 66, 67]. Specifically, Eq. 17 at time $t + \Delta t$ is expressed as:

$$\boldsymbol{M}\ddot{\boldsymbol{d}}_{t+\Delta t} + \boldsymbol{C}\dot{\boldsymbol{d}}_{t+\Delta t} + \boldsymbol{K}\boldsymbol{d}_{t+\Delta t} + \boldsymbol{S}\boldsymbol{\lambda}_{t+\Delta t} = \boldsymbol{f}_{t+\Delta t} \tag{18a}$$

$$\boldsymbol{S}^{\top}\boldsymbol{d}_{t+\Delta t} = \boldsymbol{0} \tag{18b}$$

The displacement and velocity vectors are updated as [68, 69]:

$$\boldsymbol{d}_{t+\Delta t} = \boldsymbol{q}^0 + \left(\beta\Delta t^2\right)\ddot{\boldsymbol{d}}_{t+\Delta t} \quad \text{where,} \quad \boldsymbol{q}^0 = \boldsymbol{d}_t + \Delta t\dot{\boldsymbol{d}}_t + \frac{(\Delta t)^2}{2}\left(1-2\beta\right)\ddot{\boldsymbol{d}}_t \tag{19a}$$

$$\text{and} \quad \dot{\boldsymbol{d}}_{t+\Delta t} = \boldsymbol{q}^1 + \left(\gamma\Delta t\right)\ddot{\boldsymbol{d}}_{t+\Delta t} \quad \text{where,} \quad \boldsymbol{q}^1 = \dot{\boldsymbol{d}}_t + \Delta t\left(1-\gamma\right)\ddot{\boldsymbol{d}}_t \tag{19b}$$

where the Newmark paramters β and γ are set to $\beta = 0.25$ and $\gamma = 0.5$ [68, 69, 70, 71].

Substituting Eq. 19 in Eq. 18, we arrive at:

$$\begin{bmatrix} \boldsymbol{M} + \left(\gamma\Delta t\right)\boldsymbol{C} + \left(\beta\Delta t^2\right)\boldsymbol{K} & \boldsymbol{S} \\ \left(\beta\Delta t^2\right)\boldsymbol{S}^{\top} & \boldsymbol{0} \end{bmatrix} \begin{Bmatrix} \ddot{\boldsymbol{d}}_{t+\Delta t} \\ \hat{\boldsymbol{\lambda}}_{t+\Delta t} \end{Bmatrix} = \begin{Bmatrix} \boldsymbol{f}_{t+\Delta t} - \boldsymbol{K}\boldsymbol{q}^0 - \boldsymbol{M}\boldsymbol{q}^1 \\ -\boldsymbol{S}^{\top}\boldsymbol{q}^0 \end{Bmatrix}. \tag{20}$$

that must be solved at each time step. Observe that when the mesh does not contain any tangled elements, Eq. 20 reduces to (standard FEM):

$$\left[\boldsymbol{M} + \left(\gamma\Delta t\right)\boldsymbol{C} + \left(\beta\Delta t^2\right)\boldsymbol{K}\right]\ddot{\boldsymbol{d}}_{t+\Delta t} = \boldsymbol{f}_{t+\Delta t} - \boldsymbol{K}\boldsymbol{q}^0 - \boldsymbol{M}\boldsymbol{q}^1 \tag{21}$$

Here, the expressions for $\boldsymbol{M}$, $\boldsymbol{K}$ and $\boldsymbol{f}$ (Eq. 13 to Eq. 15) also reduce to that of the standard FEM.

3.4. Free vibration

If no damping or forcing terms exist, Eq. 17 reduces to:

$$\boldsymbol{M}\ddot{\boldsymbol{d}} + \boldsymbol{K}\boldsymbol{d} + \boldsymbol{S}\hat{\boldsymbol{\lambda}} = \boldsymbol{0} \tag{22a}$$

$$\boldsymbol{S}^{\top}\boldsymbol{d} = \boldsymbol{0} \tag{22b}$$

In free vibration analysis, $\boldsymbol{d}(\boldsymbol{x},t)$ can be expressed as $\boldsymbol{d}(\boldsymbol{x},t)=\bar{\boldsymbol{d}}(\boldsymbol{x})\sin(\omega t)$, where ω is the frequency and $\bar{\boldsymbol{d}}$ is the eigenvector. Thus, Eq. 22 reduces to:

$$-\omega^2\boldsymbol{M}\bar{\boldsymbol{d}}+\boldsymbol{K}\bar{\boldsymbol{d}}+\boldsymbol{S}\hat{\boldsymbol{\lambda}}=\boldsymbol{0} \tag{23a}$$

$$\boldsymbol{S}^\top\bar{\boldsymbol{d}}=\boldsymbol{0} \tag{23b}$$

Thus, one must solve the following Eigen system:

$$\begin{bmatrix}\boldsymbol{K} & \boldsymbol{S}\\ \boldsymbol{S}^\top & \boldsymbol{0}\end{bmatrix}\begin{Bmatrix}\bar{\boldsymbol{d}}\\ \hat{\boldsymbol{\lambda}}\end{Bmatrix}=\omega^2\begin{bmatrix}\boldsymbol{M} & \boldsymbol{0}\\ \boldsymbol{0} & \boldsymbol{0}\end{bmatrix}\begin{Bmatrix}\bar{\boldsymbol{d}}\\ \hat{\boldsymbol{\lambda}}\end{Bmatrix}. \tag{24}$$

4. Implementation

We now discuss the implementation of the proposed methodology.

4.1. Computing the Stiffness Matrix

Consider again the two-element mesh in Fig. 4. According to Eq. 14, the elemental stiffness matrix associated with the non-tangled element E_2 is:

$$\boldsymbol{k}_2=\int_{C_2^+}\left(\nabla\boldsymbol{N}_2^{+\top}\boldsymbol{D}\nabla\boldsymbol{N}_2^+\right)d\Omega \tag{25}$$

Since $C_2^+=E_2$, $\boldsymbol{k}_2$ can be computed numerically via standard Gauss integration, i.e.,

$$\boldsymbol{k}_2=\int_{-1}^{1}\int_{-1}^{1}\left(\boldsymbol{J}^{-1}\nabla_{\boldsymbol{\xi}}\boldsymbol{N}_2\right)^\top\boldsymbol{D}\left(\boldsymbol{J}^{-1}\nabla_{\boldsymbol{\xi}}\boldsymbol{N}_2\right)|\boldsymbol{J}|d\xi_1 d\xi_2. \tag{26}$$

where, $|\boldsymbol{J}|$ represents the determinant of the Jacobian matrix ($\boldsymbol{J}$). On the other hand, the stiffness matrix $\boldsymbol{k}_1$ associated with the tangled element E_1 is given by (see Eq. 14):

$$\boldsymbol{k}_1=\int_{C_1^+}\left(\nabla\boldsymbol{N}_1^{+\top}\boldsymbol{D}\nabla\boldsymbol{N}_1^+\right)d\Omega\quad-\int_{C_1^-}\left(\nabla\boldsymbol{N}_1^{-\top}\boldsymbol{D}\nabla\boldsymbol{N}_1^-\right)d\Omega \tag{27}$$

Recall that C_1^+ (C_1^-) gets mapped to the J^+ (J^-) region of the parametric space (see Fig. 2c). Accordingly, the differential area for the positive component is given by:

$$d\Omega=dx_1dx_2=|\boldsymbol{J}|d\xi_1d\xi_2 \tag{28}$$

On the other hand, the differential area for the negative component is given by:

$$d\Omega=dx_1dx_2=-|\boldsymbol{J}|d\xi_1d\xi_2 \tag{29}$$

Accordingly, the two terms of $\boldsymbol{k}_1$ are given by:

$$\int_{C_1^+}\left(\nabla\boldsymbol{N}_1^{+\top}\boldsymbol{D}\nabla\boldsymbol{N}_1^+\right)d\Omega=\int_{J^+}\left(\boldsymbol{J}^{-1}\nabla_{\boldsymbol{\xi}}\boldsymbol{N}_1^+\right)^\top\boldsymbol{D}\left(\boldsymbol{J}^{-1}\nabla_{\boldsymbol{\xi}}\boldsymbol{N}_1^+\right)|\boldsymbol{J}|d\xi_1d\xi_2 \tag{30}$$

and

$$\int_{C_1^-} \left(\nabla \boldsymbol{N}_1^{-\top} \boldsymbol{D} \nabla \boldsymbol{N}_1^-\right) d\Omega = -\int_{J^-} \left(\boldsymbol{J}^{-1}\nabla_{\boldsymbol{\xi}} \boldsymbol{N}_1^-\right)^\top \boldsymbol{D} \left(\boldsymbol{J}^{-1}\nabla_{\boldsymbol{\xi}} \boldsymbol{N}_1^-\right) |\boldsymbol{J}| d\xi_1 d\xi_2 \tag{31}$$

Thus,

$$\boldsymbol{k}_1 = \int_{J^+} \left(\boldsymbol{J}^{-1}\nabla_{\boldsymbol{\xi}} \boldsymbol{N}_1^+\right)^\top \boldsymbol{D} \left(\boldsymbol{J}^{-1}\nabla_{\boldsymbol{\xi}} \boldsymbol{N}_1^+\right) |\boldsymbol{J}| d\xi_1 d\xi_2 + \int_{J^-} \left(\boldsymbol{J}^{-1}\nabla_{\boldsymbol{\xi}} \boldsymbol{N}_1^-\right)^\top \boldsymbol{D} \left(\boldsymbol{J}^{-1}\nabla_{\boldsymbol{\xi}} \boldsymbol{N}_1^-\right) |\boldsymbol{J}| d\xi_1 d\xi_2. \tag{32}$$

When the two terms on RHS are grouped together, they represent the entire parametric space of the tangled element, i.e., $J^+ \cup J^- = [-1, 1]^2$. The fact that entire parametric space is now considered enables us to use standard Gauss integration, albeit with the sign of the Jacobian determinant included, i.e., one should not use the absolute value of the Jacobian determinant, but its signed value. This results in

$$\boldsymbol{k}_1 = \int_{J^+ \cup J^-} \left(\boldsymbol{J}^{-1}\nabla_{\boldsymbol{\xi}} \boldsymbol{N}_1\right)^\top \boldsymbol{D} \left(\boldsymbol{J}^{-1}\nabla_{\boldsymbol{\xi}} \boldsymbol{N}_1\right) |\boldsymbol{J}| d\xi_1 d\xi_2. \tag{33}$$

Thus, to obtain the elemental stiffness matrix in i-TFEM, standard Gauss integration can be employed for both regular and tangled elements, but the sign of the Jacobian must be retained. In many FEM implementations, the absolute value of the Jacobian determinant is used, and this will lead to erroneous results. The mass matrix and the forcing terms are computed similarly. It was shown in [72] that decomposing the domain into positive and negative Jacobian regions is equivalent (in terms of accuracy and convergence) to numerically integrating over the element domain.

In addition to the stiffness and the mass matrices, the constraint matrix must be included in i-TFEM formulation as discussed next. If all the Gauss points lie in the positive Jacobian region, then standard FEM is valid, and there is no need for additional constraints.

4.2. Constraint Enforcement

Next, consider the constraint matrix $\boldsymbol{S}$ in Eq. 16. Recall that the choice of $\boldsymbol{N}^\lambda$ depends on the element type, i.e., $\boldsymbol{N}$. For Q9 elements, where the primary field $\boldsymbol{u}$ is approximated using standard biquadratic functions $\boldsymbol{N}$, we select linear functions $\boldsymbol{N}^\lambda$ to approximate $\boldsymbol{\lambda}$. This choice of the $\boldsymbol{N}^\lambda$ satisfies the following conditions [68]: (a) $\boldsymbol{S}$ is full-ranked, and (b)

$$n_u \geq n_\lambda \tag{34}$$

where, n_u and n_λ are the number of unknown degrees of the primary variable $\boldsymbol{u}$ and the Lagrange variable $\boldsymbol{\lambda}$ respectively.

For the two-element Q9 mesh depicted in Fig. 4a, the k^{th} column-group of $\boldsymbol{S}$ is given by:

$$\boldsymbol{S}_k = \int_{F_1} [\![\boldsymbol{N}_1(\boldsymbol{p})]\!]^\top \boldsymbol{N}_k^\lambda(\boldsymbol{p})\, d\Omega \tag{35}$$

where $\boldsymbol{p}$ denotes a point within the fold F_1 and $\boldsymbol{N}_k^\lambda$ is the k^{th} group of $\boldsymbol{N}^\lambda$. The number of columns in each group is equal to the number of degrees of freedom per node. Computing Eq. 35 involves integration

over the *non-convex* region (F_1) which can be challenging and computationally expensive [53]. To overcome this issue, we employ a point-collocation approach [68, 73]. Point collocation has been used in several FEM formulations where such constraints arise [74, 75, 76, 77, 78], and will be discussed next.

For the 2-element mesh, recall that the compatibility constraint (Eq. 3) implies that for any point $\boldsymbol{p}$ inside F_1:

$$[\![\boldsymbol{N}_1(\boldsymbol{p})]\!]\boldsymbol{d}_1 = 0 \quad \text{i.e.,} \quad \left(\boldsymbol{N}_1^+(\boldsymbol{p}) - \boldsymbol{N}_1^-(\boldsymbol{p})\right)\boldsymbol{d}_1 = 0 \tag{36}$$

Consider three noncollinear points ($\boldsymbol{p}_1$, $\boldsymbol{p}_2$, and $\boldsymbol{p}_3$) located in the fold (see Fig. 5).

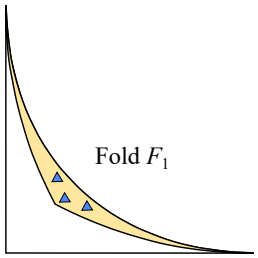

Figure 5: Three noncollinear points within the overlapping region.

By evaluating $[\![\boldsymbol{N}_1(\cdot)]\!]$ at these points, we can construct a matrix $\overline{\boldsymbol{S}}$, where the k^{th} column-group of $\overline{\boldsymbol{S}}$ is given by

$$\overline{\boldsymbol{S}}_k = [\![\boldsymbol{N}_1(\boldsymbol{p}_k)]\!]^\top \tag{37}$$

From Eq. 36

$$\overline{\boldsymbol{S}}^\top \boldsymbol{d} = \boldsymbol{0}. \tag{38}$$

While the matrices $\boldsymbol{S}$ and $\overline{\boldsymbol{S}}$ are different, observe the similarities: (a) they both satisfy the compatibility constraints and (b) their columns are linearly independent, i.e., $\text{rank}(\overline{\boldsymbol{S}}) = \text{rank}(\boldsymbol{S}) = n_\lambda$ ($= 6$ in this case).

Therefore, we replace the $\boldsymbol{S}$ matrix in Eq. 17 with $\overline{\boldsymbol{S}}$. This leads to a different set of Lagrange multipliers $\bar{\boldsymbol{\lambda}}$, but this is acceptable since $\boldsymbol{\lambda}$ itself is not of importance here. Thus, the integration over the overlapping region can be completely avoided.

For Q9 elements, the number of constraint equations is equal to 3 $\times$ degree(s) of freedom per node per tangled element. Hence for elastodynamics, the number of constraint equations required is 6 per tangled Q9 element. To construct the $\overline{\boldsymbol{S}}$ matrix for Q9 elements, Eq. 37 is evaluated at three non-collinear points ($\boldsymbol{p}_1$, $\boldsymbol{p}_2$, and $\boldsymbol{p}_3$) located inside the overlapping region (preferably away from the $|\boldsymbol{J}| = 0$ curve). Recall that any point $\boldsymbol{p}_k$ within the fold can be mapped to two points $\boldsymbol{a}_k$ and $\boldsymbol{b}_k$ in the parametric space, belonging to the regions J^- and J^+ respectively. Thus, for each point $\boldsymbol{p}_k$, we have

$$\overline{\boldsymbol{S}}_k = \left(\boldsymbol{N}_1^+(\boldsymbol{p}_k) - \boldsymbol{N}_1^-(\boldsymbol{p}_k)\right)^\top = \left(\boldsymbol{N}_1(\boldsymbol{b}_k) - \boldsymbol{N}_1(\boldsymbol{a}_k)\right)^\top \tag{39}$$

The methodology for finding $\boldsymbol{a}_k$ and $\boldsymbol{b}_k$ is discussed below.

For a tangled element E_j, a list $\mathcal{L}$ of Gauss points with negative Jacobian is generated. If the number of points in $\mathcal{L}$ are less than 3, the remaining J^- points are searched from the Gauss quadrature rule with

successively higher number of points. For instance, if the standard Gauss quadrature of 3×3 includes two Gauss points in J^- region, the remaining point is searched from 4×4 Gauss quadrature points. If no point is found, higher quadrature rule is employed until three unique $\boldsymbol{a}_k$ points in J^- are obtained. For the examples considered in this paper, we had search for no more than 5×5 Gauss points.

Once three $\boldsymbol{a}_k$ points are found, the corresponding points $\boldsymbol{p}_k$ in the physical space can be computed using the basis functions:

$$\boldsymbol{p}_k = \boldsymbol{N}_j(\boldsymbol{a}_k)\hat{\boldsymbol{x}}_j \tag{40}$$

where $\hat{\boldsymbol{x}}_j$ is the position vector for the nodes of the element E_j. Once the physical point $\boldsymbol{p}_k$ belonging to the fold is obtained, the corresponding point $\boldsymbol{b}_k \in J^+$ can be obtained via the Newton-Raphson method. Finally, Eq. 37 can be employed to compute the constraint matrix.

This simple procedure to compute the constraint matrix alleviates the need to explicitly identify the boundary of the tangled region. Note that the number of constraints must not exceed the recommended number (3×2 in this case), else it may lead to over-constraining the element, or locking.

4.3. Multiple Overlaps

Thus far, the overlapping region was shared by only one neighboring non-tangled element. However, in practice, the overlapping region may be shared by multiple non-tangled elements as illustrated in Fig. 6. In this case, three non-tangled elements E_2, E_3, and E_4 intersect with the overlapping region of the tangled element E_1. However, this does not change the methodology. For example, the total area is given by:

$$\int\limits_{E_1+E_2+E_3+E_4} d\Omega = \int\limits_{C_1^+} d\Omega + \int\limits_{C_2^+} d\Omega + \int\limits_{C_3^+} d\Omega + \int\limits_{C_4^+} d\Omega - \int\limits_{C_1^-} d\Omega \tag{41}$$

i.e., the integral over the negative component must be subtracted once. Furthermore, the field compatibility equation is as before:

$$[\![\boldsymbol{u}_1]\!] = 0 \quad \text{in } F_1 \tag{42}$$

Consequently, the stiffness and mass matrices, forcing vectors, and constraint matrix are computed as before: (1) standard stiffness matrices $\boldsymbol{k}_i$, $i = 1, \ldots, 4$ are computed for all elements using standard Gauss integration while retaining the sign of the Jacobian (the mass matrices and forcing vectors are computed similarly), and (2) the constraint matrix is computed by evaluating Eq. 37 at (any) three points within each fold F_j.

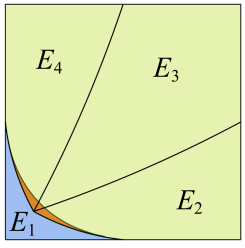

Figure 6: Overlapping region shared by multiple non-tangled elements; central nodes are not shown to avoid clutter.

4.4. Extension to Other Element Types

We now consider the extension of the above framework to other element types, specifically, 2D 4-node quadrilateral (Q4) and 3D 8-node hexahedral (H8) elements.

First, consider a four-node tangled quadrilateral (Q4) (Fig. 7a). The parametric space of this element is shown in Fig. 7b and Fig. 7c shows the overlapping region of the tangled Q4 element. The concepts discussed for Q9 elements directly apply here as well except that only one constraint equation is needed per tangled element since the dimension of the primary field has reduced.

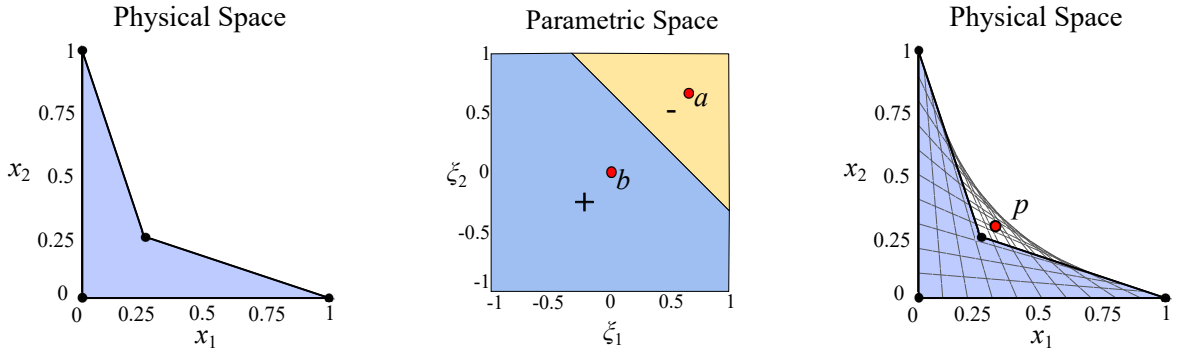

Figure 7: (a) A tangled Q4 element. (b) Parametric space of the concave element. Parametric space can be divided into positive and negative Jacobian regions. (c) Physical space of the tangled Q4 element along with tangled region.

Next, consider a 3D 8-node hexahedral element in Fig. 8a. Observe that the element is non-convex. Fig. 8b shows the positive and negative Jacobian regions of the parametric space. Here too, the parametric mapping becomes non-invertible and the element is said to be tangled. The corresponding overlapping region is shown in Fig. 8c. Here again, the displacement field being (tri)linear, we require one constraint per tangled element.

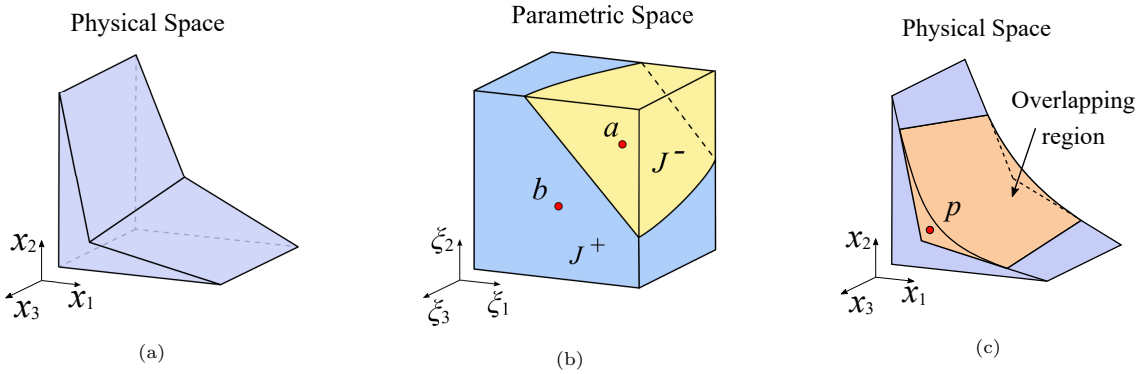

Figure 8: (a) A tangled hexahedral element. (b) Parametric space of the tangled element. Parametric space can be divided into positive and negative Jacobian regions. (c) The overlapping region (fold) of the tangled element.

In summary, for both Q4 and H8 elements, to obtain the constraint matrix, we need to consider only one

point in the tangled region and evaluate Eq. 37 at that point.

5. Numerical Experiments

The use of tangled meshes for free and forced vibration analysis is verified using the proposed i-TFEM framework. Numerical experiments are conducted under the following conditions:

- The implementation is in MATLAB R2022a, on a standard Windows 10 desktop with Intel(R) Core(TM) i9-9820X CPU running at 3.3 GHz with 16 GB memory.
- The standard Gaussian quadrature is employed for all elements; that is, 2×2 for Q4, 3×3 for Q9, and $2 \times 2 \times 2$ for H8.
- In standard FEM, the absolute value of Jacobian determinant is employed (to be consistent with commercial FEM systems such as ANSYS). Without the absolute value, and without the constraint, standard FEM can lead to nonsensical results [51].

5.1. Cantilever Problem

Consider the cantilever beam in Fig. 9 with dimensions $L = 200$ mm, $h = 10$ mm, and $b = 10$ mm. The material properties are: Young's modulus $E = 45.36$ GPa, Poisson's ratio $\nu = 0.25$, and mass density $\rho = 7397$ kg/m^3. This problem is discussed in [40], and is investigated here using Q4, Q9, and H8 tangled elements.

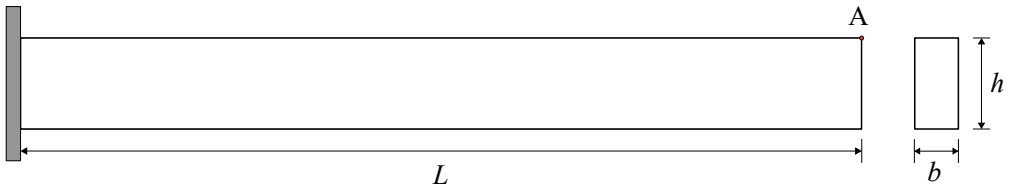

Figure 9: A cantilever beam problem.

5.1.1. 2D cantilever: Mesh Construction

The beam is first modeled as a plane stress problem. We consider tangled and non-tangled (regular) meshes for both 4-node (Q4) and 9-node (Q9) elements. The number of elements is controlled by a mesh-index N, where the number of elements in the regular mesh is $20N \times N$. The corresponding tangled mesh is created by replacing each element by a pair of elements (one of them being tangled) as illustrated in Fig. 11.

Fig. 10 illustrates a regular Q4 mesh when $N = 2$, and Fig. 11, the corresponding tangled mesh. The repeating units for both meshes are shown on the right-hand side of each figure. For the tangled mesh, the position of the re-entrant vertex R can be varied using the parameter $d \in (0, 0.5)$ where $d = 1/3$ in Fig. 11.

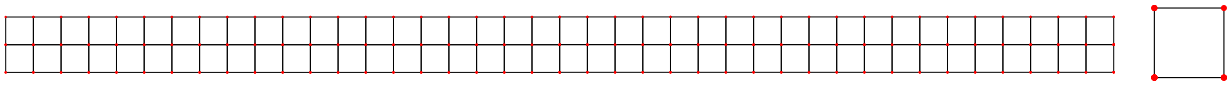

Figure 10: Regular Q4 mesh with $N = 2$

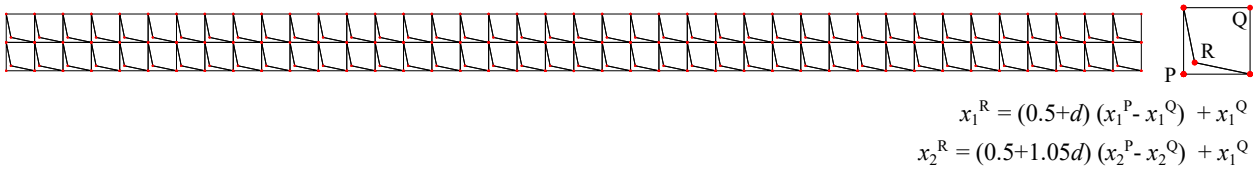

Figure 11: Tangled Q4 mesh with $N = 2$.

The repeating units for regular and tangled Q9 meshes are illustrated in Fig. 12a and Fig. 12b respectively. Note the interior edges have a slight curvature. The extent of tangling is once again controlled by d.

(a) (b)

Figure 12: Q9 repeating unit for (a) regular (b) tangled meshes.

5.1.2. 2D Cantilever: Convergence of Natural Frequencies

We now compare the natural frequencies of the cantilever computed from three different methods: standard FEM over regular mesh, standard FEM over tangled mesh, and i-TFEM over tangled mesh. Using the Q4 elements, for all three methods, the first and second natural frequencies are plotted as a function of N in Fig. 13a and Fig. 13b respectively. Observe that FEM over a regular mesh and i-TFEM over the tangled mesh converge to the same value. On the other hand, FEM over a tangled mesh converges to an incorrect solution.

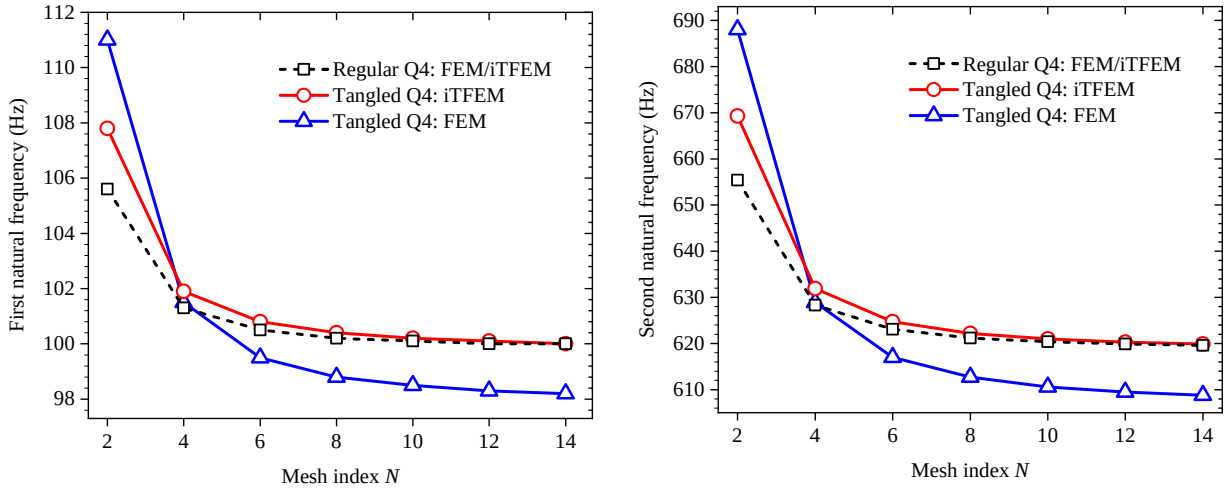

Figure 13: Convergence of (a) first and (b) second natural frequency of the cantilever computed with Q4 tangled elements.

Fig. 14 shows similar plots using Q9 elements. Here the error in standard FEM over tangled meshes is even more pronounced.

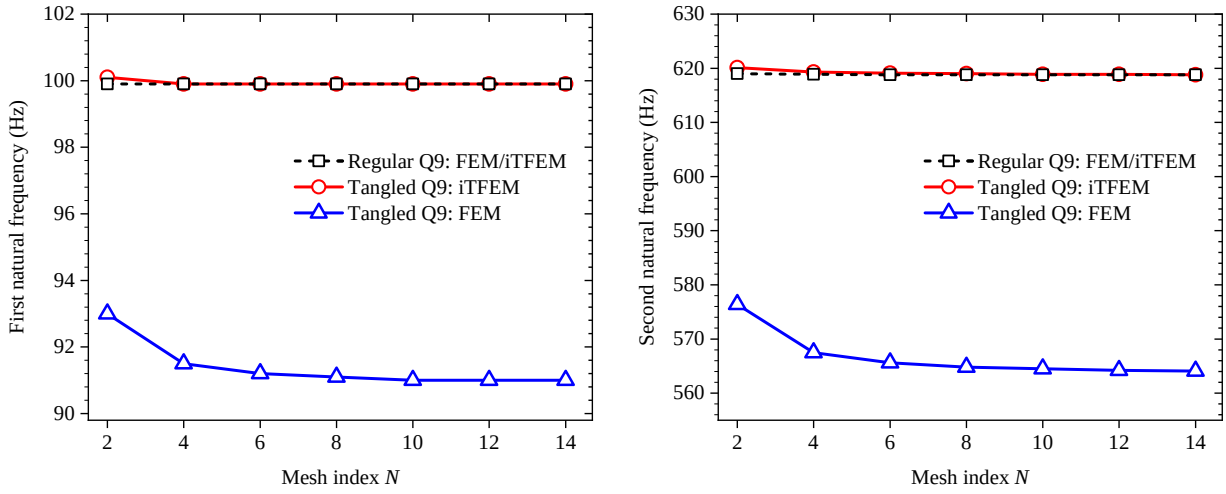

Figure 14: Convergence of (a) first and (b) second natural frequency of the cantilever computed with Q9 tangled elements.

5.1.3. 2D cantilever: Forced Vibrations

In this example, the same cantilever beam is subjected to a transient loading $f(t) = 4.54 \sin(\pi t/T)$ kN for $0 \leq t \leq T$ where T is the natural period of the cantilever (see Fig. 15). The load is applied at the top right corner of the beam (point A in Fig. 9).

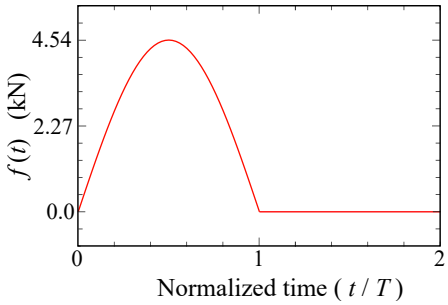

Figure 15: Transient loading for cantilever beam.

This problem is first solved using a tangled mesh with Q4 elements. Four different mesh sizes are considered: $N = 2, 3, 4$, and 8. The vertical displacement of the cantilever tip v_A is plotted with respect to time as normalized/dimensionless parameters $v_A EI/L^3$ and t/T respectively in Fig. 16, where $I = bh^3/12$ is the second moment of inertia. Note that this problem uses the same parameters given at the beginning of Section 5.1. But, for completeness, they are repeated here: $L = 200$ mm, $h = 10$ mm, and $b = 10$ mm, $E = 45.36$ GPa, $\rho = 7397$ kg/m^3, $\nu = 0.25$. The reference solution is obtained using a regular Q9 mesh of size 160×8 ($N = 8$). As one can observe, i-TFEM converges to the reference solution as the mesh discretization is increased.

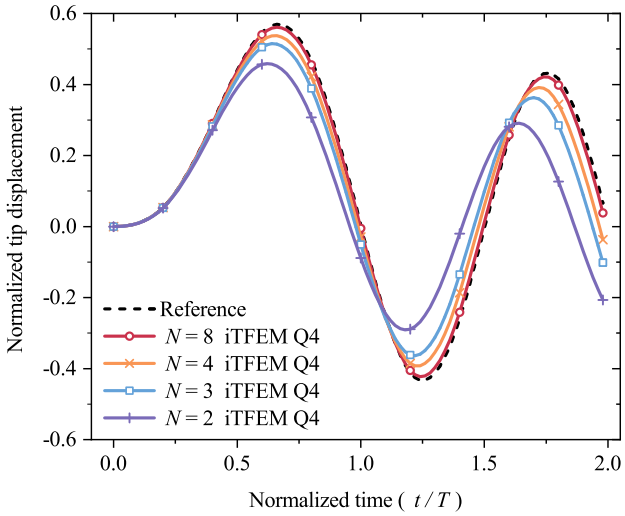

Figure 16: Convergence for the tangled Q4 meshes using i-TFEM.

Next, for the mesh size of $N = 8$, we compare the solutions obtained by the three methods: FEM and i-TFEM using the tangled mesh and FEM using untangled mesh. The normalized tip displacements obtained using the three methods are plotted in Fig. 17a for Q4 elements, and Fig. 17b for Q9 elements. Observe that the response obtained using i-TFEM (over the tangled mesh) matches with that obtained over the regular mesh. However, FEM over the tangled mesh leads to incorrect results.

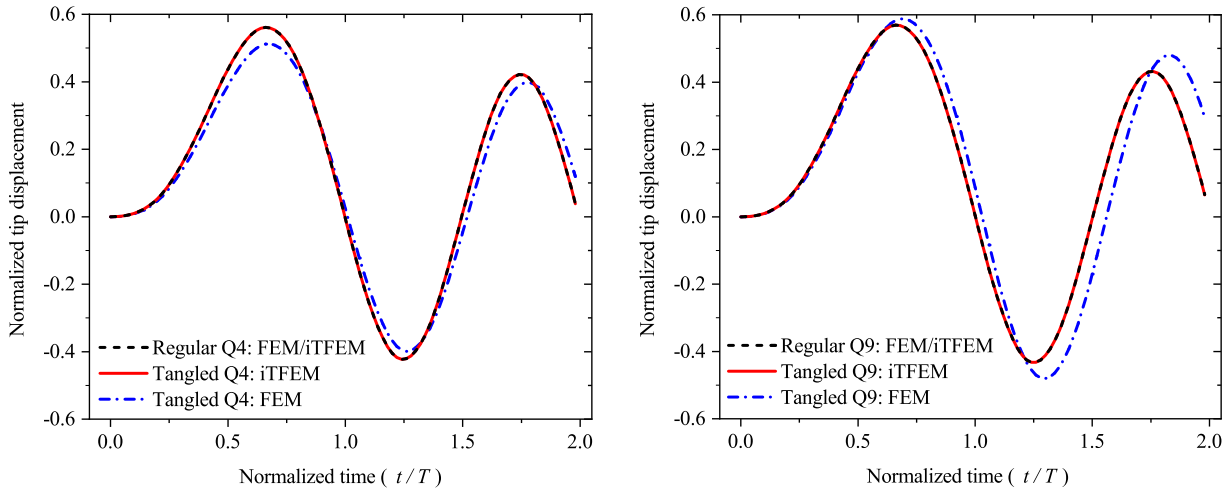

(a) (b)

Figure 17: Comparison of i-TFEM and FEM solutions with $N = 8$ mesh using (a) Q4 and (b) Q9 elements.

5.1.4. 2D Cantilever Beam: Degree of Tangling

In the above study, the extent of tangling was fixed with $d = 0.4$. Next, we study the effect of tangling parameter d for a fixed mesh size $N = 2$. Fig. 18a plots the i-TFEM solution for various values of d. Observe that as the tangling increases (i.e. as d increases), the i-TFEM solution approaches the result obtained by the corresponding regular mesh.

To compare the performance of FEM and i-TFEM, we plot the maximum value of normalized tip displacement for $d \in [0, 0.499]$ in Fig. 18b. Observe that for $d < 0.2$, i-TFEM solution matches FEM solution for the tangled mesh. The Jacobian at all the Gauss points are positive and i-TFEM reduces to the standard FEM. For $d \geq 0.2$, Jacobian is negative at one or more Gauss points. As $d \in [0.2, 0.499]$ increases, i-TFEM results approach the results obtained by employing the regular mesh. On the other hand, FEM solutions increasingly move farther away from those obtained using regular mesh.

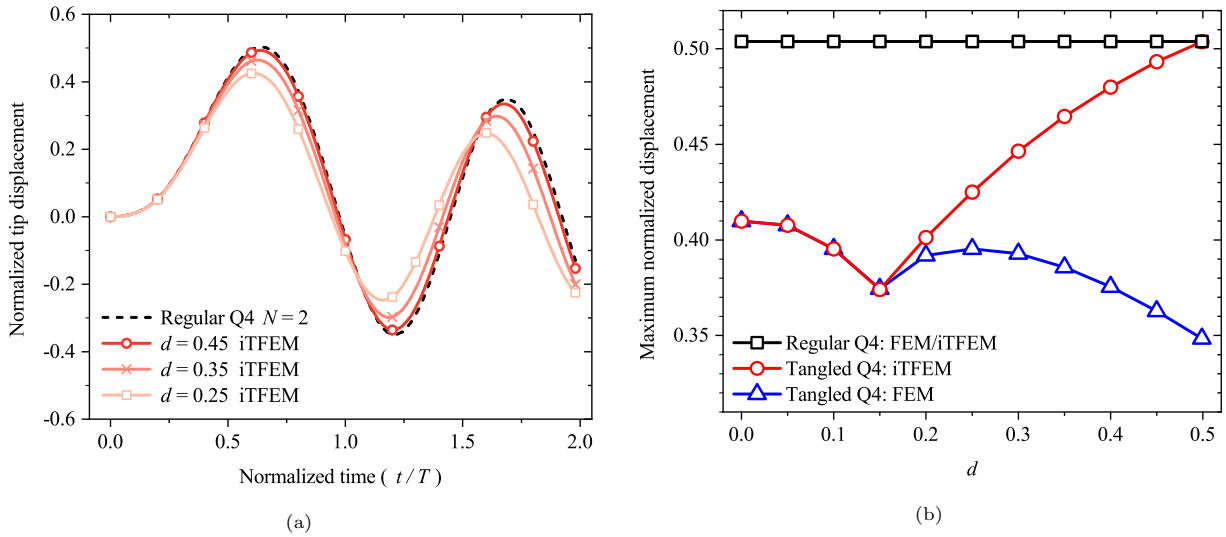

(a) (b)

Figure 18: Solutions obtained using Q4 mesh with mesh index $N = 2$ to study the effect of varying the extent of tangling.

5.1.5. 3D cantilever: Mesh Construction

Next, we discretize the 3D cantilever using regular and tangled meshes. A regular mesh with $60 \times 3 \times 3$ elements is shown in Fig. 19.

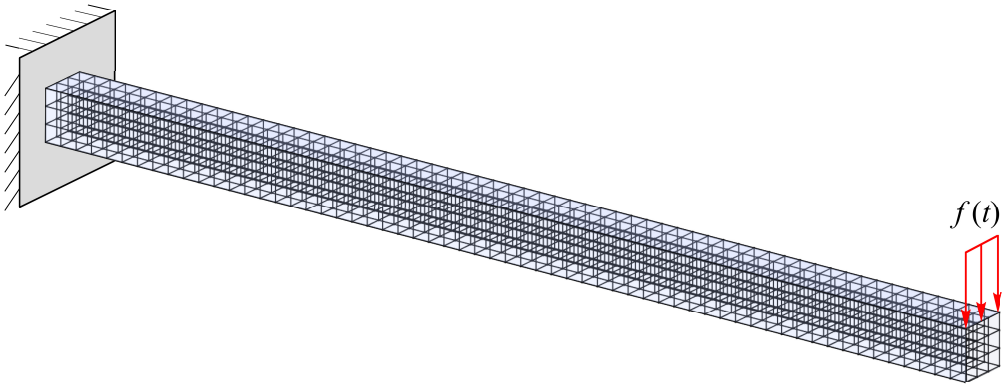

Figure 19: Regular H8 mesh with $N = 1$

The regular repeating unit consists of $3 \times 3 \times 3$ elements as shown in Fig. 20a. The tangled repeating unit is constructed by modifying the non-tangled unit in two steps:

1. We convert each element of the regular mesh into a 2-element unit, as depicted in Fig. 20b, resulting in 54 elements. Positions of the new re-entrant nodes (nodes 9 and 10) are given as

$$x_3^{(9)} = x_3^{(1)}, \qquad x_i^{(9)} = x_i^{(1)} + (0.5 - d)\, s_i, \quad i = 1, 2 \tag{43a}$$

$$x_3^{(10)} = x_3^{(5)}, \qquad x_i^{(10)} = x_i^{(5)} + (0.6 - d)\, s_i, \quad i = 1, 2 \tag{43b}$$

where s_i is the element size in i^{th} direction and the parameter d controls the extent of tangling (discussed later).

2. We then move the node B (highlighted in red in Fig. 20a), using the same parameter d, towards the left-hand side.

$$\boldsymbol{x}_d^{(B)} = \boldsymbol{x}^{(B)} - d \times [1.75s_1 \quad 1.75s_2 \quad 0.7s_3]^\top. \tag{44a}$$

The value of the parameter d can be varied from 0 to 0.48. The front view of a resulting tangled mesh for $d = 0.4$ is illustrated in Fig. 20c.

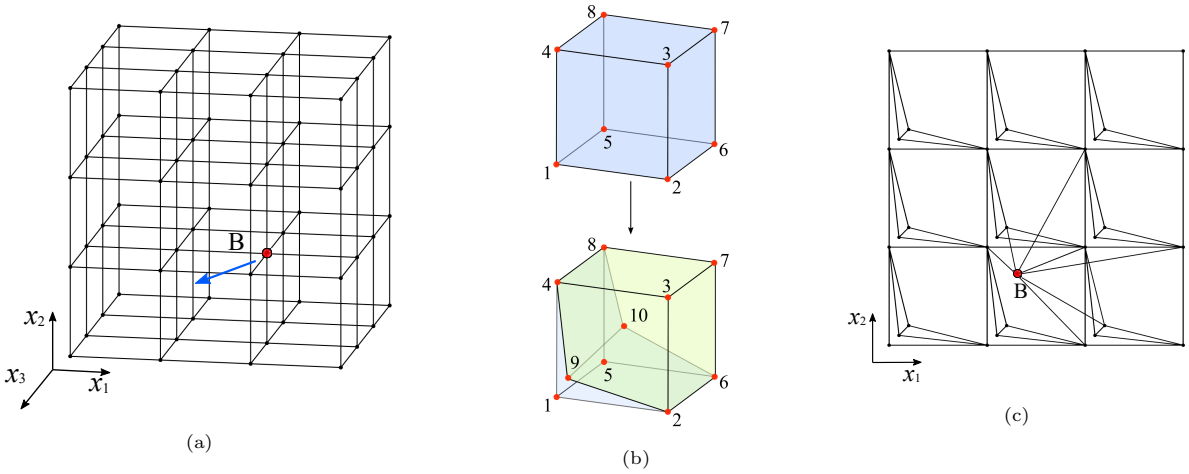

Figure 20: (a) Regular mesh (b) Non-tangled element converted to tangled element (c) Front view of the tangled mesh.

The tangled mesh unit (Fig. 20c) has 54 elements; out of which 28 elements are tangled. Fig. 21 illustrates some of the tangled elements. These elements are non-convex with non-planar faces.

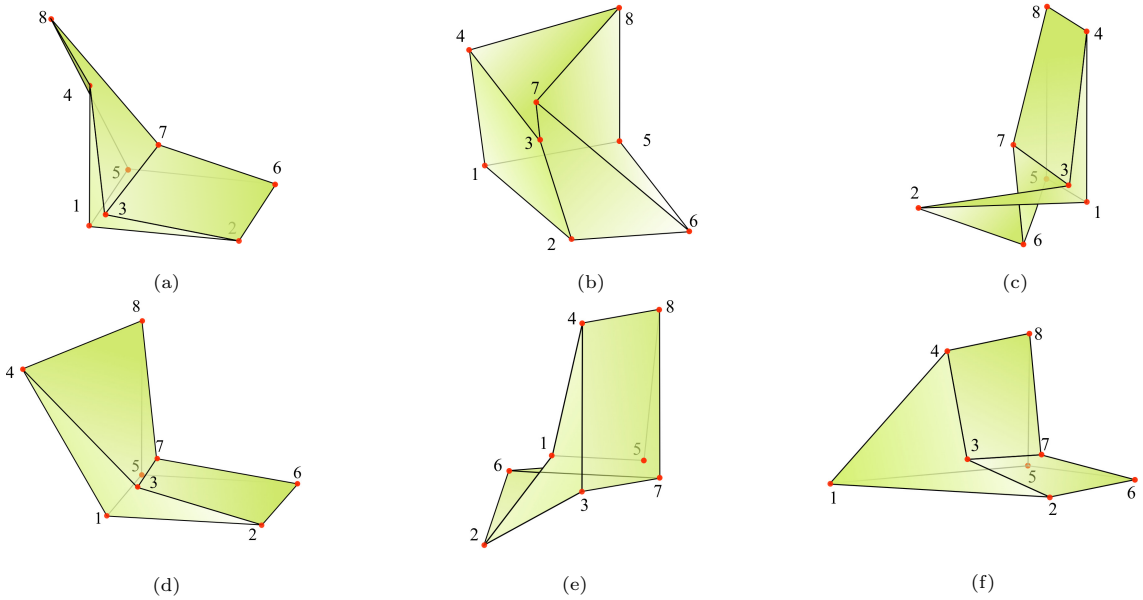

Figure 21: Some tangled elements present in the mesh shown in Fig. 20c

5.1.6. 3D cantilever: Forced Vibration

We perform forced vibration analysis of the 3D cantilever beam as described in section 5.1.3. To discretize the domain, N number of cubic repeating units described above are arranged in the configuration of $(20N \times N \times N)$.

We solve this problem using the tangled meshes with $N = 1$ to 3 and $d = 0.4$. The response of the cantilever using i-TFEM is depicted in Fig. 22a. The normalized vertical displacement of the cantilever tip $v_A EI/L^3$ is plotted with respect to normalized time t/T. The reference solution is obtained by considering a regular (non-tangled) mesh with 67,500 elements. Next, for mesh with $N = 2$, Fig. 22b compares the solutions obtained by the three methods: FEM and i-TFEM using the tangled mesh and FEM using untangled mesh. We can observe similar convergence and trends as in the 2D problem.

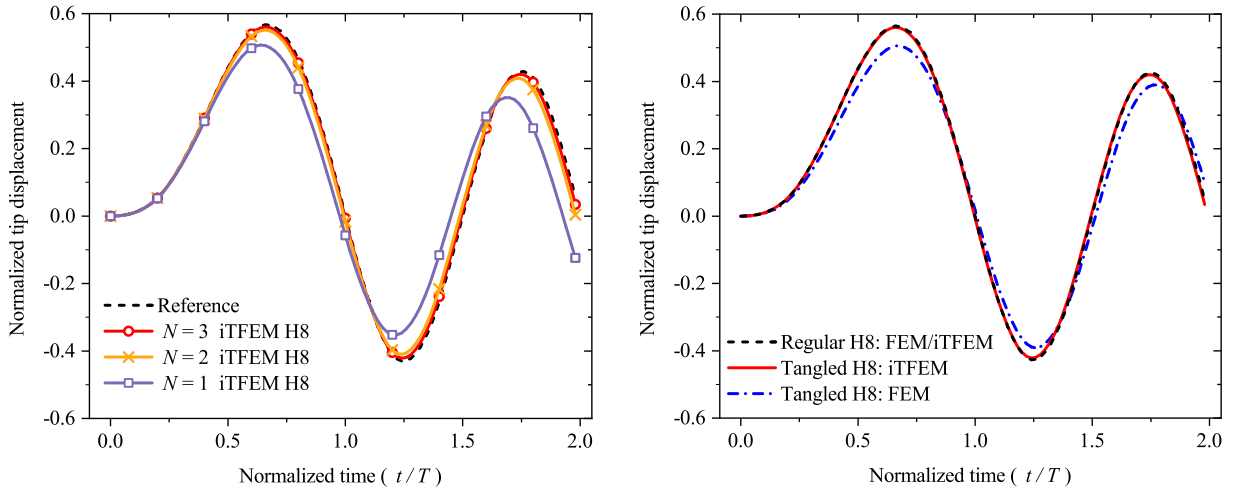

Figure 22: (a) Convergence for tangled hexahedral (H8) meshes using i-TFEM (b) Comparison of i-TFEM and FEM solutions obtained using hexahedral meshes with the size $N = 2$.

5.1.7. 3D Cantilever: Degree of Tangling

In the above study, the extent of tangling was fixed with $d = 0.4$. Here, we study the effect of tangling on the computed solutions by varying d from change 0 to 0.48 for a fixed mesh size, with $N = 2$. Once again, as d increases, the i-TFEM solution approaches the reference solution as illustrated in Fig. 23a. Next, we plot the maximum normalized displacement obtained using i-TFEM (over tangled mesh) and FEM (obtained over regular and tangled mesh) in Fig. 23b. As seen in the 2D example, FEM deviates from the expected results with an increase in d, as opposed to i-TFEM.

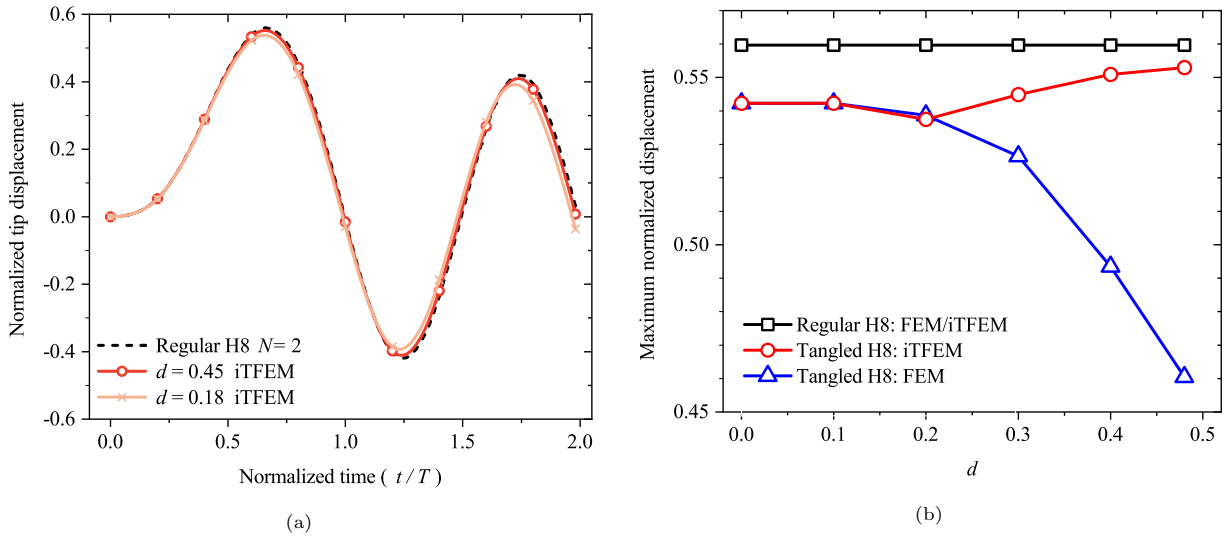

Figure 23: Solutions with hexahedral (H8) $N = 2$ mesh to study the effect of varying the extent of tangling.

5.2. Spherical Shell with Damping

Next, we investigate the damping of a spherical shell subjected to a concentrated load as illustrated in Fig. 24. The problem has been previously investigated in [79]. The geometric parameters of the shell are as follows: inner radius = 120 mm, thickness = 1 mm, and outer chord radius $c = 22.9$ mm. A concentrated load $f(t) = 0.1\cos(0.05t)$ kN is applied at the apex while the outer surface is fixed along the thickness. Rayleigh damping coefficients are $\alpha_1 = 0.005$, $\alpha_2 = 0.272$ while other material parameters are $E = 1000$ GPa, $\rho = 10^4$ kg/m^3, and $\nu = 0.3$.

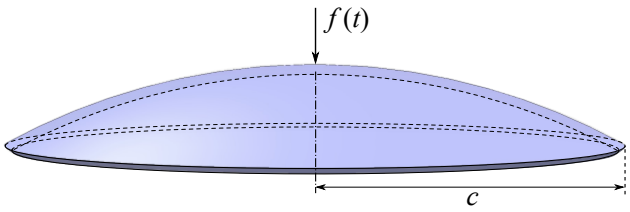

Figure 24: Spherical shell geometry

Due to axisymmetric nature of the shell, it is modeled in 2D as shown in Fig. 25. The mesh for this example is constructed by using the 4-element mesh as the basic repeating unit, as in Fig. 25. The extent of tangling can be varied by the parameter $d \in [0, 0.5]$. For $d = 0$, a regular mesh is obtained. As d increases, one out of the four elements gets tangled. In this experiment, tangled mesh is constructed with $d = 0.475$ and has 40×4 Q9 elements.

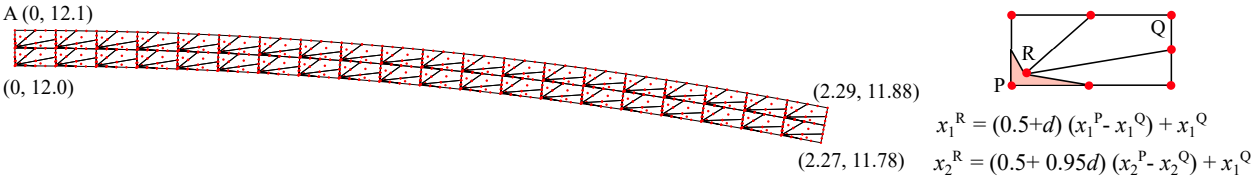

Figure 25: Spherical shell with Q9 elements with straight edges.

The apex (point A in Fig. 25) displacement with respect to time is plotted in Fig. 26. Once again, the solution obtained using i-TFEM with the tangled mesh closely matches the solution obtained using the regular mesh.

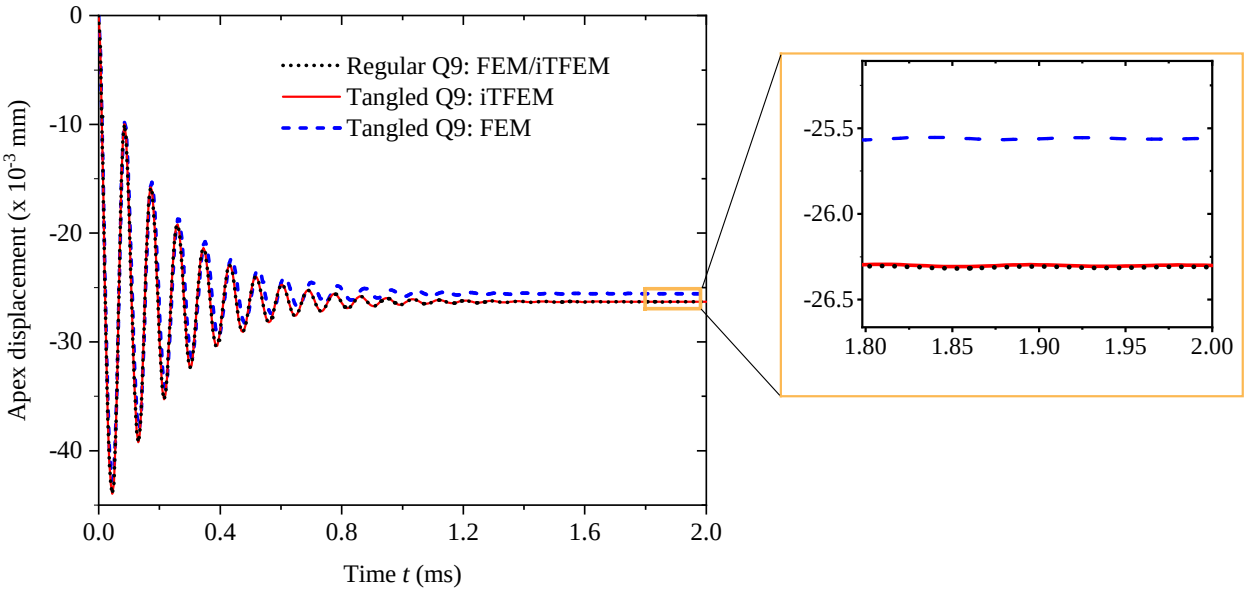

Figure 26: Transient responses of the spherical shell subjected to a harmonic loading.

5.3. 3D real world tangled meshes: Free Vibration

Finally, we consider real-world tangled meshes illustrated in Fig. 27 (provided in [3]) where the tangled elements are highlighted in red color. Although it is feasible to untangle these meshes [3], the use of i-TFEM eliminates the need for untangling.

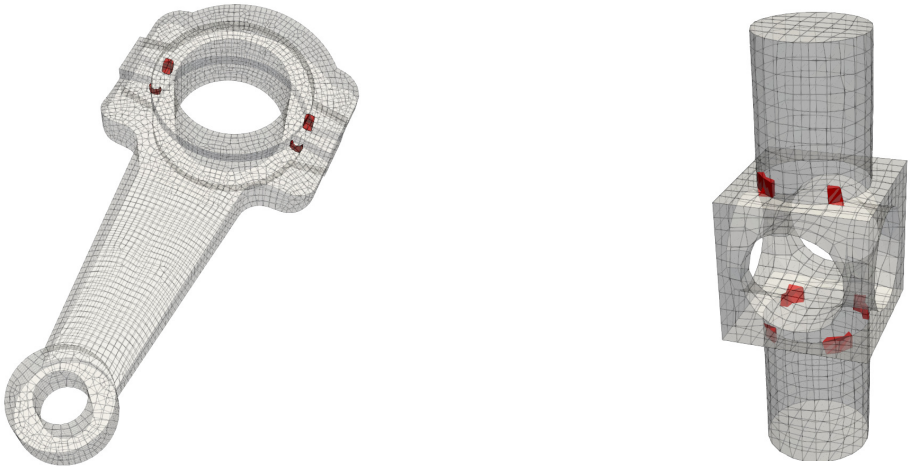

(a) (b)

Figure 27: Tangled mesh of (a) linking rod and (b) block provided by [3]. Tangled elements are highlighted in red.

For free vibration analysis, we consider the following material properties: $E = 673$ GPa, $\rho = 5759$ kg/m^3, and $\nu = 0.28$. For the linking rod, the inner surface of the smaller hole is fixed, while the bottom face is fixed for the block. The first mode deformation obtained by employing i-TFEM is visualized in Fig. 28.

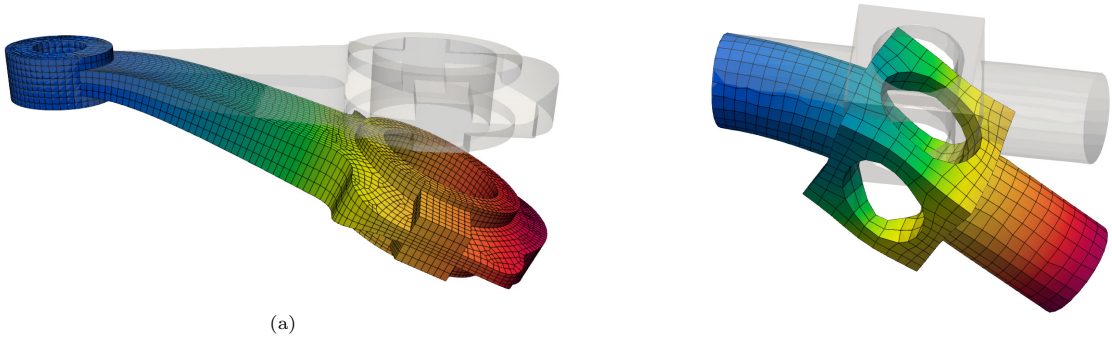

(a) (b)

Figure 28: The first mode deformation for (a) linking rod and (b) block; obtained using i-TFEM.

Table 1 compares the first four natural frequencies obtained via i-TFEM using the tangled mesh with those obtained using the untangled mesh. It can be observed that the natural frequencies obtained from both methods are comparable, and the additional computational time required for i-TFEM is minimal. The time required to untangle the mesh is not included. Note that the tangled meshes in Fig. 27a and Fig. 27b are generated using multi-sweep [80] and PolyCube [12] respectively.

Table 1: Comparison of solutions over tangled and untangled meshes provided in [3].

Model [3]	Mesh	$\lvert \boldsymbol{J} \rvert_{\min}$	No. of Tangled Hexahedra	Natural frequency (Hz) 1	2	3	4	Time (seconds)
linking rod	tangled	-0.39	8/11316	6.370	15.536	28.819	68.998	17.167
	untangled	0.55	0/11316	6.361	15.533	28.790	68.907	17.137
block	tangled	-0.70	10/2520	1542	1544	5604	6539	3.549
	untangled	0.25	0/2520	1547	1548	5584	6731	3.520

Finally, we consider the tangled meshes generated by other state-of-the-art hex meshing algorithms: frame-field [81] and semi-manual dual sheet [7] approach. These methods resulted in the tangled meshes in Fig. 29a and Fig. 29b respectively. The mesh data was obtained from Hexalab repository [82]. I-TFEM was employed to compute the vibration modes over these tangled meshes. Table 2 provides the computational time required for i-TFEM as well as FEM (albeit with inaccurate results). Observe that the computational overhead due to i-TFEM is within 3% of the FEM simulation time.

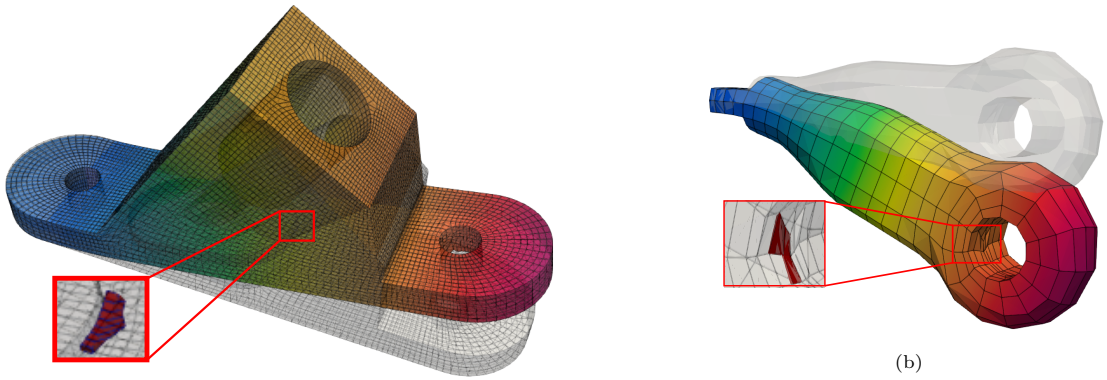

(a) (b)

Figure 29: The first mode deformation for (a) i02u_m2 [81] and (b) rod [7] ; obtained using i-TFEM.

Table 2: Time comparison with i-TFEM and FEM for real-world tangled meshes.

Model	$\lvert \boldsymbol{J} \rvert_{\min}$	No. of Tangled Hexahedra	Natural frequency (Hz) 1	2	3	4	Time (seconds) i-TFEM	FEM (incorrect)
i02u_m2 [81]	-0.41	7/37800	12.1	27.3	58.4	159.6	95.684	92.716
rod [7]	-0.59	3/704	514.8	636.0	2989.8	5659.7	0.527	0.519

5.4. Need for constraints

Recall that i-TFEM requires the field compatibility constraints to be enforced. To underline the significance of constraints, a free vibration analysis of a cantilever beam is conducted. The cantilever beam (see Fig. 9) with following parameters is considered [83, 84, 85]: $L = 100$ mm, $h = 10$ mm, $b = 1$ mm, $E = 205.9$ GPa, $\rho = 7845$ kg/m^3, $\nu = 0.3$. A plane stress condition is assumed. The tangled Q9 mesh is created using the repeating unit shown in Fig. 12b. The resulting vibration modes, both with and without imposition of compatibility constraints, are displayed in Fig. 30 and Fig. 31 respectively. Notably, no spurious modes occur with the application of constraints. However, spurious modes appear in the absence of constraints as illustrated in Fig. 31.

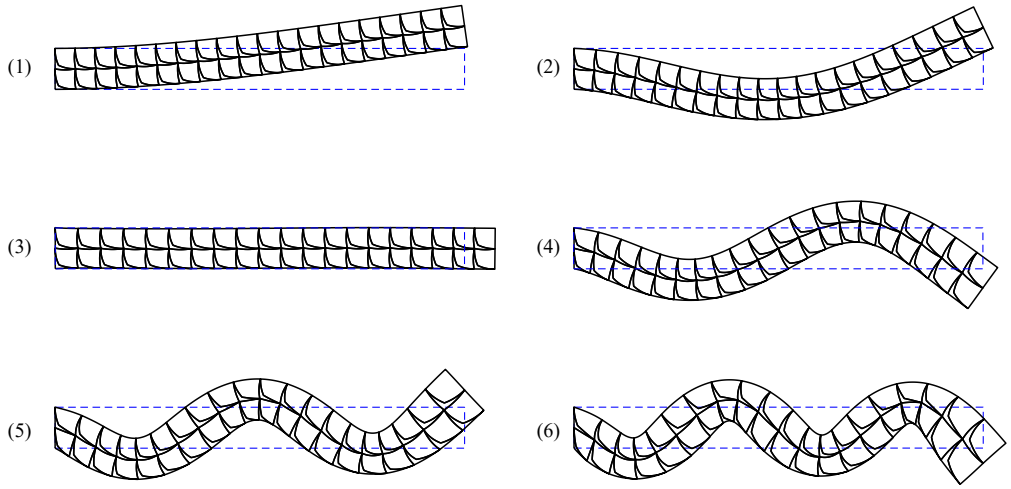

Figure 30: First 6 modes of the cantilever beam obtained with constraints.

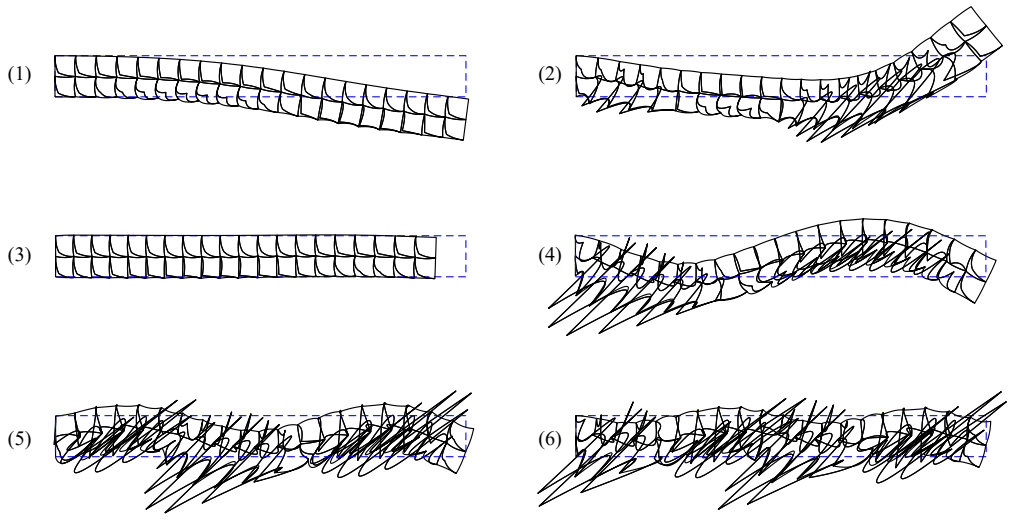

Figure 31: First 6 modes of the cantilever beam obtained without incorporating constraints.

6. Conclusions

In conclusion, the presence of tangled (non-convex) elements in standard finite element meshes can lead to erroneous results. In this paper, we have proposed the isoparametric tangled finite element method (i-TFEM) to handle tangled elements for free and forced vibration problems. The proposed i-TFEM is demonstrated for 4-node (Q4), 9-node (Q9) quadrilateral, and 8-node hexahedral (H8) elements.

By treating the positive and negative Jacobian regions separately, variational formulation for i-TFEM is derived for elastodynamics. This leads to a simple modification of the standard FEM stiffness and mass matrices and the inclusion of piece-wise compatibility constraints. Specifically, the stiffness and mass matrices in i-TFEM can be computed as in standard FEM, but the sign of the Jacobian determinant is retained during integration. To enforce compatibility over the fold, a constraint matrix $\boldsymbol{S}$ must be constructed by sampling the shape functions at n_c points within the fold, where $n_c = 1$ for Q4 and H8 elements, and $n_c = 3$ for a Q9 elements.

Finally, numerous examples are presented to demonstrate that i-TFEM consistently handles tangled elements and produces reliable solutions. The time required for i-TFEM is found to be almost identical to that for standard FEM in practical scenarios.

In this work, degenerate elements, where the Jacobian is equal to zero at a Gauss point, are not considered since zero-Jacobian value causes singularity in the stiffness matrix. Moreover, fully inverted elements, which have negative Jacobian at *all* the Gauss points are also not considered in this paper. Such elements will be addressed in future work.

Acknowledgments

The authors would like to thank the support of National Science Foundation through grant 1715970.

References

[1] T. J. Hughes, J. A. Cottrell, Y. Bazilevs, Isogeometric analysis: Cad, finite elements, nurbs, exact geometry and mesh refinement, Computer Methods in Applied Mechanics and Engineering 194 (39-41) (2005) 4135–4195.

[2] S. Bhowmick, S. M. Shontz, Towards high-quality, untangled meshes via a force-directed graph embedding approach, Procedia Computer Science 1 (1) (2010) 357–366.

[3] M. Livesu, A. Sheffer, N. Vining, M. Tarini, Practical hex-mesh optimization via edge-cone rectification, ACM Transactions on Graphics 34 (4) (2015) 1–11.

[4] J. Sarrate, A. Huerta, Efficient unstructured quadrilateral mesh generation, International Journal for Numerical Methods in Engineering 49 (10) (2000) 1327–1350.

[5] N. Pietroni, M. Campen, A. Sheffer, G. Cherchi, D. Bommes, X. Gao, R. Scateni, F. Ledoux, J. Remacle, M. Livesu, Hex-mesh generation and processing: a survey, ACM Transactions on Graphics 42 (2) (2022) 1–44.

[6] S. Bonaretti, C. Seiler, C. Boichon, M. Reyes, P. Büchler, Image-based vs. mesh-based statistical appearance models of the human femur: implications for finite element simulations, Medical Engineering & Physics 36 (12) (2014) 1626–1635.

[7] K. Takayama, Dual sheet meshing: An interactive approach to robust hexahedralization, in: Computer Graphics Forum, Vol. 38, Wiley Online Library, 2019, pp. 37–48.

[8] M. Livesu, N. Pietroni, E. Puppo, A. Sheffer, P. Cignoni, Loopycuts: Practical feature-preserving block decomposition for strongly hex-dominant meshing, ACM Transactions on Graphics 39 (4) (2020) 121–1.

[9] M. Mandad, R. Chen, D. Bommes, M. Campen, Intrinsic mixed-integer polycubes for hexahedral meshing, Computer Aided Geometric Design 94 (2022) 102078.

[10] X. Fang, W. Xu, H. Bao, J. Huang, All-hex meshing using closed-form induced polycube, ACM Transactions on Graphics 35 (4) (2016) 1–9.

[11] M. Livesu, N. Vining, A. Sheffer, J. Gregson, R. Scateni, Polycut: Monotone graph-cuts for polycube base-complex construction, ACM Transactions on Graphics 32 (6) (2013) 1–12.

[12] J. Gregson, A. Sheffer, E. Zhang, All-hex mesh generation via volumetric polycube deformation, in: Computer Graphics Forum, Vol. 30, Wiley Online Library, 2011, pp. 1407–1416.

[13] H. Liu, P. Zhang, E. Chien, J. Solomon, D. Bommes, Singularity-constrained octahedral fields for hexahedral meshing., ACM Transactions on Graphics 37 (4) (2018) 93–1.

[14] T. Jiang, J. Huang, Y. Wang, Y. Tong, H. Bao, Frame field singularity correctionfor automatic hexahedralization, IEEE Transactions on Visualization and Computer Graphics 20 (8) (2013) 1189–1199.

[15] Y. Li, Y. Liu, W. Xu, W. Wang, B. Guo, All-hex meshing using singularity-restricted field, ACM Transactions on Graphics 31 (6) (2012) 1–11.

[16] M. Nieser, U. Reitebuch, K. Polthier, Cubecover–parameterization of 3d volumes, in: Computer Graphics Forum, Vol. 30, Wiley Online Library, 2011, pp. 1397–1406.

[17] J. Huang, Y. Tong, H. Wei, H. Bao, Boundary aligned smooth 3d cross-frame field, ACM transactions on Graphics 30 (6) (2011) 1–8.

[18] P. M. Knupp, A method for hexahedral mesh shape optimization, International Journal for Numerical Methods in Engineering 58 (2) (2003) 319–332.

[19] S. Leger, A. Pepin, An updated lagrangian method with error estimation and adaptive remeshing for very large deformation elasticity problems: The three-dimensional case, Computer Methods in Applied Mechanics and Engineering 309 (2016) 1–18.

[20] V. Vavourakis, D. Loukidis, D. C. Charmpis, P. Papanastasiou, Assessment of remeshing and remapping strategies for large deformation elastoplastic finite element analysis, Computers & Structures 114 (2013) 133–146.

[21] M. L. Staten, S. J. Owen, S. M. Shontz, A. G. Salinger, T. S. Coffey, A comparison of mesh morphing methods for 3d shape optimization, in: Proceedings of the 20th International Meshing Roundtable, Springer, 2011, pp. 293–311.

[22] Q. Huang, W.-X. Zhang, Q. Wang, L. Liu, X.-M. Fu, Untangling all-hex meshes via adaptive boundary optimization, Graphical Models 121 (2022) 101136.

[23] K. Xu, X. Gao, G. Chen, Hexahedral mesh quality improvement via edge-angle optimization, Computers & Graphics 70 (2018) 17–27.

[24] M. N. Akram, L. Si, G. Chen, An embedded polygon strategy for quality improvement of 2d quadrilateral meshes with boundaries., in: VISIGRAPP (1: GRAPP), 2021, pp. 177–184.

[25] M. Reberol, K. Verhetsel, F. Henrotte, D. Bommes, J.-F. Remacle, Robust topological construction of all-hexahedral boundary layer meshes, ACM Transactions on Mathematical Software 49 (1) (2023) 1–32.

[26] J. F. Shepherd, C. R. Johnson, Hexahedral mesh generation constraints, Engineering with Computers 24 (3) (2008) 195–213.

[27] P. M. Knupp, Hexahedral and tetrahedral mesh untangling, Engineering with Computers 17 (3) (2001) 261–268.

[28] G. Liu, K. Dai, T. T. Nguyen, A smoothed finite element method for mechanics problems, Computational Mechanics 39 (6) (2007) 859–877.

[29] L. Zhang, K.-T. Kim, K.-J. Bathe, The new paradigm of finite element solutions with overlapping elements in cad–computational efficiency of the procedure, Computers & Structures 199 (2018) 1–17.

[30] K.-T. Kim, K.-J. Bathe, Accurate solution of wave propagation problems in elasticity, Computers & Structures 249 (2021) 106502.

[31] S. Lee, K.-J. Bathe, Solution of the generalized eigenvalue problem using overlapping finite elements, Advances in Engineering Software 173 (2022) 103241.

[32] M. S. Floater, Mean value coordinates, Computer Aided Geometric Design 20 (1) (2003) 19–27.

[33] G. Manzini, A. Russo, N. Sukumar, New perspectives on polygonal and polyhedral finite element methods, Mathematical Models and Methods in Applied Sciences 24 (08) (2014) 1665–1699.

[34] H. Chi, C. Talischi, O. Lopez-Pamies, G. H. Paulino, Polygonal finite elements for finite elasticity, International Journal for Numerical Methods in Engineering 101 (4) (2015) 305–328.

[35] A. Rand, A. Gillette, C. Bajaj, Interpolation error estimates for mean value coordinates over convex polygons, Advances in Computational Mathematics 39 (2) (2013) 327–347.

[36] L. Beirão da Veiga, F. Brezzi, A. Cangiani, G. Manzini, L. D. Marini, A. Russo, Basic principles of virtual element methods, Mathematical Models and Methods in Applied Sciences 23 (01) (2013) 199–214.

[37] A. L. Gain, C. Talischi, G. H. Paulino, On the virtual element method for three-dimensional linear elasticity problems on arbitrary polyhedral meshes, Computer Methods in Applied Mechanics and Engineering 282 (2014) 132–160.

[38] G. H. Paulino, A. L. Gain, Bridging art and engineering using escher-based virtual elements, Structural and Multidisciplinary Optimization 51 (4) (2015) 867–883.

[39] H. Chi, L. B. Da Veiga, G. Paulino, Some basic formulations of the virtual element method (vem) for finite deformations, Computer Methods in Applied Mechanics and Engineering 318 (2017) 148–192.

[40] K. Park, H. Chi, G. H. Paulino, On nonconvex meshes for elastodynamics using virtual element methods with explicit time integration, Computer Methods in Applied Mechanics and Engineering 356 (2019) 669–684.

[41] S. Rajendran, K. Liew, A novel unsymmetric 8-node plane element immune to mesh distortion under a quadratic displacement field, International Journal for Numerical Methods in Engineering 58 (11) (2003) 1713–1748.

[42] S. Rajendran, A technique to develop mesh-distortion immune finite elements, Computer Methods in Applied Mechanics and Engineering 199 (17-20) (2010) 1044–1063.

[43] C. Jiang, Z.-Q. Zhang, X. Han, G.-R. Liu, Selective smoothed finite element methods for extremely large deformation of anisotropic incompressible bio-tissues, International Journal for Numerical Methods in Engineering 99 (8) (2014) 587–610.

[44] W. Zeng, G. Liu, Smoothed finite element methods: an overview and recent developments, Archives of Computational Methods in Engineering 25 (2) (2018) 397–435.

[45] M. L. Cascio, A. Milazzo, I. Benedetti, Virtual element method for computational homogenization of composite and heterogeneous materials, Composite Structures 232 (2020) 111523.

[46] D. van Huyssteen, F. L. Rivarola, G. Etse, P. Steinmann, On mesh refinement procedures for the virtual element method for two-dimensional elastic problems, Computer Methods in Applied Mechanics and Engineering 393 (2022) 114849.

[47] S. Huo, G. Liu, J. Zhang, C. Song, A smoothed finite element method for octree-based polyhedral meshes with large number of hanging nodes and irregular elements, Computer Methods in Applied Mechanics and Engineering 359 (2020) 112646.

[48] S. Natarajan, S. P. Bordas, E. T. Ooi, Virtual and smoothed finite elements: a connection and its application to polygonal/polyhedral finite element methods, International Journal for Numerical Methods in Engineering 104 (13) (2015) 1173–1199.

[49] B. Prabhune, K. Suresh, On why mesh untangling may not be required, Engineering with Computers (2023) 1–18.

[50] B. Prabhune, K. Suresh, A computationally efficient isoparametric tangled finite element method for handling inverted quadrilateral and hexahedral elements, Computer Methods in Applied Mechanics and Engineering 405 (2023) 115897.

[51] B. Prabhune, K. Suresh, Isoparametric tangled finite element method for nonlinear elasticity, arXiv preprint arXiv:2303.10799 (2023).

[52] B. Prabhune, K. Suresh, Towards tangled finite element analysis over partially inverted hexahedral elements, arXiv preprint arXiv:2207.03905 (2022).

[53] B. Prabhune, S. Sridhara, K. Suresh, Tangled finite element method for handling concave elements in quadrilateral meshes, International Journal for Numerical Methods in Engineering 123 (7) (2022) 1576–1605.

[54] A. Eriksson, A. Nordmark, Constrained stability of conservative static equilibrium, Computational Mechanics 64 (2019) 1199–1219.

[55] B. Dhas, A. R. Srinivasa, J. Reddy, D. Roy, A novel four-field mixed fe approximation for kirchhoff rods using cartan's moving frames, Computer Methods in Applied Mechanics and Engineering (2022) 115094.

[56] T. H. Pian, Finite element formulation by variational principles with relaxed continuity requirements, in: The mathematical foundations of the finite element method with applications to partial differential equations, Elsevier, 1972, pp. 671–687.

[57] P. Tong, New displacement hybrid finite element models for solid continua, International Journal for Numerical Methods in Engineering 2 (1) (1970) 73–83.

[58] C. Farhat, F.-X. Roux, A method of finite element tearing and interconnecting and its parallel solution algorithm, International Journal for Numerical Methods in Engineering 32 (6) (1991) 1205–1227.

[59] J. T. Oden, J. N. Reddy, Variational methods in theoretical mechanics, Springer Science & Business Media, 2012.

[60] F. Auricchio, L. B. da Veiga, F. Brezzi, C. Lovadina, Mixed finite element methods, Encyclopedia of Computational Mechanics Second Edition (2017) 1–53.

[61] N. J. Carpenter, R. L. Taylor, M. G. Katona, Lagrange constraints for transient finite element surface contact, International Journal for Numerical Methods in Engineering 32 (1) (1991) 103–128.

[62] K.-J. Bathe, A. Chaudhary, A solution method for planar and axisymmetric contact problems, International Journal for Numerical Methods in Engineering 21 (1) (1985) 65–88.

[63] T. J. Hughes, R. L. Taylor, J. L. Sackman, A. Curnier, W. Kanoknukulchai, A finite element method for a class of contact-impact problems, Computer Methods in Applied Mechanics and Engineering 8 (3) (1976) 249–276.

[64] N. M. Newmark, A method of computation for structural dynamics, Journal of the Engineering Mechanics Division 85 (3) (1959) 67–94.

[65] K.-J. Bathe, G. Noh, Insight into an implicit time integration scheme for structural dynamics, Computers & Structures 98 (2012) 1–6.

[66] D. F. Rossi, W. G. Ferreira, W. J. Mansur, A. F. G. Calenzani, A review of automatic time-stepping strategies on numerical time integration for structural dynamics analysis, Engineering Structures 80 (2014) 118–136.

[67] W. Kim, Higher-order explicit time integration methods for numerical analyses of structural dynamics, Latin American Journal of Solids and Structures 16 (2019) e201.

[68] O. C. Zienkiewicz, R. L. Taylor, J. Z. Zhu, The finite element method: its basis and fundamentals, Elsevier, 2005.

[69] T. J. Hughes, The finite element method: linear static and dynamic finite element analysis, Courier Corporation, 2012.

[70] M. Cihan, F. Aldakheel, B. Hudobivnik, P. Wriggers, Virtual element formulation for finite strain elastodynamics, arXiv preprint arXiv:2002.02680 (2020).

[71] Y. Gu, G.-R. Liu, A meshless local petrov-galerkin (mlpg) method for free and forced vibration analyses for solids, Computational Mechanics 27 (2001) 188–198.

[72] P. Antolin, X. Wei, A. Buffa, Robust numerical integration on curved polyhedra based on folded decompositions, Computer Methods in Applied Mechanics and Engineering 395 (2022) 114948.

[73] E. Oñate, S. Idelsohn, O. Zienkiewicz, R. Taylor, A finite point method in computational mechanics. applications to convective transport and fluid flow, International Journal for Numerical Methods in Engineering 39 (22) (1996) 3839–3866.

[74] R. Kramer, P. Bochev, C. Siefert, T. Voth, An extended finite element method with algebraic constraints (xfem-ac) for problems with weak discontinuities, Computer Methods in Applied Mechanics and Engineering 266 (2013) 70–80.

[75] R. M. Kramer, P. B. Bochev, C. M. Siefert, T. E. Voth, Algebraically constrained extended edge element method (exfem-ac) for resolution of multi-material cells, Journal of Computational Physics 276 (2014) 596–612.

[76] R. M. Kramer, C. M. Siefert, T. E. Voth, P. B. Bochev, Formulation and computation of dynamic, interface-compatible whitney complexes in three dimensions, Journal of Computational Physics 359 (2018) 45–76.

[77] G. J. Wagner, W. K. Liu, Application of essential boundary conditions in mesh-free methods: a corrected collocation method, International Journal for Numerical Methods in Engineering 47 (8) (2000) 1367–1379.

[78] C.-K. C. Wu, M. E. Plesha, Essential boundary condition enforcement in meshless methods: boundary flux collocation method, International Journal for Numerical Methods in Engineering 53 (3) (2002) 499–514.

[79] Y. Li, G. Liu, A novel node-based smoothed finite element method with linear strain fields for static, free and forced vibration analyses of solids, Applied Mathematics and Computation 352 (2019) 30–58.

[80] E. Ruiz-Gironés, X. Roca, J. Sarrate, R. Montenegro, J. M. Escobar, Simultaneous untangling and smoothing of quadrilateral and hexahedral meshes using an object-oriented framework, Advances in Engineering Software 80 (2015) 12–24.

[81] P.-A. Beaufort, M. Reberol, D. Kalmykov, H. Liu, F. Ledoux, D. Bommes, Hex me if you can, in: Computer Graphics Forum, Vol. 41, Wiley Online Library, 2022, pp. 125–134.

[82] M. Bracci, M. Tarini, N. Pietroni, M. Livesu, P. Cignoni, Hexalab. net: An online viewer for hexahedral meshes, Computer-Aided Design 110 (2019) 24–36.

[83] K. Dai, G. Liu, Free and forced vibration analysis using the smoothed finite element method, Journal of Sound and Vibration 301 (3-5) (2007) 803–820.

[84] G. Liu, T. Nguyen-Thoi, K. Lam, An edge-based smoothed finite element method for static, free and forced vibration analyses of solids, Journal of Sound and Vibration 320 (4-5) (2009) 1100–1130.

[85] T. Nagashima, Node-by-node meshless approach and its applications to structural analyses, International Journal for Numerical Methods in Engineering 46 (3) (1999) 341–385.